Soil Oxygen Monitoring with Fibre Optode Sensors: Experimental Evaluation in Soil Columns under Fluctuating Water Table and Freeze Thaw Conditions

by

Tatjana Milojevic

A thesis
presented to the University of Waterloo
in fulfilment of the
thesis requirement for the degree of
Master of Science
in
Earth Sciences

Waterloo, Ontario, Canada, 2017

AUTHOR'S DECLARATION

I hereby declare that I am the sole author of this thesis. This is a true copy of my thesis, including any required final revisions, as accepted by my examiners.

I understand that my thesis may be made electronically available to the public.

ABSTRACT

The biogeochemical functioning of natural and engineered environments is closely linked to spatial and temporal variations in molecular oxygen (O_2) concentrations. A luminescence-based, *Multi-Fibre Optode* (MuFO) sensor technique was developed to measure O_2 concentrations in fully and partially water-saturated systems. The technique relies on the conversion of high-resolution digital images of sensor-emitted light into O_2 concentrations using the classical Stern-Volmer (SV) and Lehrer equations. The method was tested in two soil column experiments designed to simulate water table fluctuations (WT) and freeze-thaw cycles (FTC) under controlled conditions. The columns were filled with a homogenized mixture of peat (20 %) and sand (80 %). Depth distributions of O_2 concentration were monitored without interruption for 20 (WT experiment) and 39 days (FTC experiment), while CO_2 effluxes from the soils were measured periodically. Increases in CO_2 emission accompanied both thawing (FTC experiment) and water table drawdown (WT experiment). During freezing, O_2 levels in the unsaturated depth interval of the soil dropped by up to 20% because of more restricted gas exchanges with the atmosphere. The CO_2 pulses in the FTC experiment were therefore attributed to the build-up of respiratory CO_2 in the pore space during freezing, and its subsequent release upon thawing. In the WT experiment, the lowering (rate of 12 cm day^{-1} over 2.5 days) of the water table allowed for O_2 migration deeper into the soil, which enhanced the aerobic mineralization of peat organic matter and, consequently, increased the emission of CO_2. In both the FTC and WT experiments, the magnitude of the CO_2 pulse decreased (from 0.26 $\mu mol^2\ s^{-1}$ to 0.07 $\mu mol^2\ s^{-1}$) with each subsequent water table and freeze-thaw cycle, indicating the progressive depletion of reactive organic carbon. No degradation of optode performance and O_2 signals were observed over the entire duration of the experiments, hence supporting the long-term deployment of the sensors for continuous O_2 monitoring in field and laboratory settings.

ACKNOWLEDGEMENTS

First and foremost, I would like to thank my supervisors, Dr. Philippe Van Cappellen and Dr. Fereidoun Rezanezhad, for giving me the opportunity to complete this M.Sc. with the Ecohydrology Research Group at the University of Waterloo. I am very grateful to them for their time, patience, guidance and encouragement to further my knowledge and experience in academics.

I am grateful to Marianne Vander Griendt, for her invaluable assistance in sample analysis, sensor calibration and in setting up the soil column experiments. I would also like to extend my gratitude to Danny Oh and Stephanie Slowinski for their assistance with sample analyses. Thank you to Dr. Christina Smeaton and Dr. Chris Parsons for their assistance and advice on this work. I am grateful to Paul Johnson, Harmen Vander Heide, and Zhenwen Wang for their help in building the *Multi-Fibre Optode* system required for this research. Additionally, I would also like to extend a big thank you to the members of the Ecohydrology Research Group for all of the encouragement I have received while working on this research.

I would like to thank the funding organizations for supporting this work. Funding for the research was provided through the Canada Excellence Research Chair (CERC) Program in Ecohydrology awarded to Dr. Philippe Van Cappellen and an NSERC Discovery Grant awarded to Dr. Fereidoun Rezanezhad.

Finally, I would like to thank my wonderful family for their constant support and encouragement.

Table of Contents

LIST OF FIGURES

LIST OF TABLES

CHAPTER 1: INTRODUCTION

Molecular oxygen (O_2) availability impacts surface and subsurface environments, ranging from terrestrial to aquatic settings, by influencing carbon and nutrient cycling, mineralogy, redox conditions, contaminant behaviour and microbial activity in both natural and engineered environments (Dutta *et al.*, 2015; Torres *et al.*, 2015; Elberling *et al.*, 2011; Blossfeld *et al.*, 2011; Glud, 2008; Kangas, 2004; Precht *et al.*, 2004). As the most energetically efficient, commonly available terminal electron acceptor (TEA), O_2 is closely connected to the biogeochemical dynamics of soils (Tan, 2000) for instance: oxidation of organic carbon to HCO_3^- or CO_2 is far more energetically efficient with O_2 as the TEA compared to NO_3^-, SO_4^{2-}, or Fe(III) (LaRowe and Van Cappellen, 2011). The concentration of O_2 is an important indicator of environmental conditions and thus can be useful in environmental monitoring and in the interpretation of soil processes and conditions, such as the bioremediation of contaminated sites (Huesemann and Truex, 1996) or the performance assessment of constructed wetland performance (Wozniak and Welker, 2007; Hammer, 1989).

With the recognition of the importance of O_2, there has been significant effort committed to the development of dependable techniques for O_2 measurement (Wang and Wolfbeis, 2014; Helm *et al.*, 2012; Clark *et al.*, 2013; Stich *et al.*, 2009; Hasumoto, 2006; Amao, 2003; Carritt and Kanwisher, 1959). The standard method for measuring O_2 in natural waters is the Winkler titration (Carpenter, 1965; Winkler, 1888). The Winkler titration method is very accurate when conducted properly, however it is laborious (making it inadequate for real-time monitoring applications) and requires the use of toxic reagents (Helm *et al.*, 2012; Wang and Wolfbeis, 2014). Traditional alternatives to the Winkler titration include electroanalytical methods such as amperometry. This is the basis for the Clark-type electrode that is often used in environmental investigations. Yet this method also has shortfalls, including analyte (O_2) consumption during measurement, poor stability over long term use, as well as the limited opportunity for modification of the set-up to suit field and laboratory experiments (Wolfbeis, 2015; Bagshaw *et al.*, 2011; Taillefert *et al.*, 2000; Klimant and Wolfbeis, 1995). Other alternative techniques include conductometry, radioisotopes,

magnetic resonance, and electron resonance, but these methods are not used as frequently in environmental applications as they are often less practical and high in cost (Wolfbeis, 2015).

The most promising method to emerge in recent decades is the optical luminescence-based sensor method, in which the optical properties of an indicator change based on exposure to an analyte (Klimant *et al.*, 1997). These systems are referred to as optrodes (as the optical counterpart of the electrode) or optodes (Klimant *et al.*, 1997). As this optical method has numerous advantages over traditional methods, Wolfbeis (2015) predicts that it will overtake Clark-type electrodes in monitoring of O_2. Optode systems are superior in that they do not consume the analyte, have full reversibility, show good precision and accuracy, and can be customized in design to meet the specific spatial and temporal measurement needs of the user for a given study (Wang and Wolfbeis, 2014). Therefore, optode techniques are ideal for collection of real-time O_2 data.

Another key benefit of O_2 optode sensors is that, while they can be purchased commercially from various manufacturers (see Chapter 4), they are relatively easy to build and customize in-house and have been implemented by various researchers (*e.g.* Larsen *et al.,* 2011; Martinez-Olmos *et al*., 2011; and Staal *et al*., 2011). Optodes generally appear as planar designs or are coated onto fibre optic cables. Both methods are effective, but selected based on the spatial requirements of the investigation. For instance, planar methods enable measurement of larger surface areas and can be used in tank set-ups such as those constructed by Pretch *et al.*, (2004) and Glud *et al.*, (1996). On the other hand, the fibre design is well adapted for monitoring smaller surface areas and in-situ samples in various fields from clinical medicine (*e.g.* Chen *et al.*, 2013) to environmental research (*e.g.* Martinez-Olmos *et al.*, 2011; Klimant *et al.*, 1997). Overall, optodes hold an advantage over more traditional methods, such as the Winkler titration or amperometric approaches, in that they are affordable and can be customized to suit the spatial and temporal measurement requirements for a variety of settings.

In this study, a *Multi-Fibre Optode* (MuFO) sensing method constructed from simple, inexpensive components and operating based on light intensity quenching is presented. The

term "*Multi Fibre Optode*" was first used by Fischer and Koop-Jakobsen (2012) to describe their new O_2 sensor system, which included multiple fibre optic cables that each had an optode coating on the distal cable ends. The term is applied here since the sensor system used is also comprised of multiple fibre optic cables serving as the waveguide for excitation light to, and emission light from, the distal optode tips. The sensor was developed in this research as a tool for obtaining high resolution measurements of O_2 in soil environments.

In order to evaluate the performance of the MuFO system, it had to be tested under environmental scenarios where dynamic shifts in O_2 levels are known or most likely to occur. Dynamic hydrological and climatic drivers (such as temperature) have been shown to regulate subsurface O_2 availability, which in turn influences the microbial activity, biogeochemistry, nutrient and carbon cycling in soils (Hefting *et al.*, 2004; Rezanezhad *et al*., 2014; Jonasson *et al*., 1999; Grogan *et al*., 2004; Henry, 2007; Matzner and Borken, 2008; Joseph and Henry, 2008; Hayashi, 2013). Thus, to evaluate the MuFO system performance, two soil column experiments were designed to simulate water table fluctuations (WT) and freeze-thaw cycles (FTC) under controlled conditions. High resolution O_2 time series data were collected from multiple depths in the soil columns filled with a homogenized artificial soil mixture comprised of 20 % peat and 80 % sand.

In the first column experiment (WT), temporal change in O_2 is examined under changing soil water content, imposed by repeated movement of the water table between the top and the bottom of the soil column. This hydrologic regime was selected to test if the MuFO can be used to distinguish the variation of O_2 levels between saturated and unsaturated zones. A large variation in O_2 levels was anticipated because the gaseous diffusion coefficient is about 10^4 times larger in air than in water (Cussler, 1997). In fact, soil water content (saturated vs unsaturated soil) is often used as a proxy in delineating subsurface redox conditions in terms of general oxic and anoxic zones in soil (Ouyang, 1990).

The second column experiment was designed to examine the O_2 distributions in seasonally-frozen soils. Cycles of freezing and thawing were imposed on the soil column through controlled variation of surface air temperature between -10 °C and +10 °C. For this, a novel soil column system was used, which was uniquely designed to better replicate natural

conditions in a controlled laboratory setting. There have been previous freeze-thaw studies with soil columns in controlled laboratory settings (*e.g.,* Teepe and Ludwig, 2004; Hentschel *et al*., 2008; Yu *et al*., 2011), however, to our knowledge, no soil studies have continuously monitored O_2 within a soil profile experiencing cycles of freezing and thawing. This research is novel in that regard.

While O_2 saturation (% relative to atmospheric O_2) at various depths within each column was monitored under the changing temperature and hydrologic conditions, the evolution of carbon dioxide (CO_2) in the soil column headspace during both experiments was also monitored and characterized. The emission of CO_2 to the atmosphere under varying hydrologic and climatic conditions has been a focus of much research (*e.g.,* Teepe and Ludwig, 2004; Chimner and Cooper, 2003; Aerts and Ludwig, 1997; Moore and Dalva, 1993), though, in many cases concurrent O_2 dynamics are not collected (*e.g.*, Miao *et al*., 2013; Ouyang and Zheng, 2000; Blodau and Moore, 2003). Yet, the merits of incorporating measurements of both gases have not gone unrecognized. For instance, Angert *et al*. (2015) successfully used O_2 and CO_2 concentration measurements in a well-drained soil to calculate the soil apparent respiratory quotient (ARQ). Turcu *et al*. (2005) noted that understanding of soil microbial activity can be improved by observing CO_2 production, in conjunction with O_2 consumption, as this can indicate the type of soil respiration (aerobic versus anaerobic) occurring. Additionally, changes in hydrological regimes affecting the redox potential in the subsurface (of which O_2 availability is a major factor) directly impact biogeochemical processes affecting soil respiration (Hefting *et al.*, 2004; Rezanezhad *et al*., 2014). The data of CO_2 monitored here was mainly intended to serve as an indicator of ongoing soil respiration and gas transport under the imposed hydrologic and air temperature regimes. Notably, autotrophic respiration (*e.g.* by plant metabolism) was excluded for simplicity of design, but is recognized as an important source of CO_2 (Högberg *et al.,* 2001).

Gas concentrations in the atmosphere and dissolved in water are affected by temperature, pressure, and salinity (Benson *et al.*, 1980 and 1984). In the soil ecosystem, gas fluxes and migration in the pore space are closely linked to soil water content and soil temperature (Ouyang and Zheng, 2000). Thus, the concentrations of O_2 and CO_2 in the pore space of the

soil environment would similarly be influenced by these factors, which were investigated independently in the two soil column experiments presented.

In the WT experiment, the soil fluctuated between a saturated and unsaturated state. As the soil became saturated with water, decreasing the ability of gas to diffuse throughout the pore space, it was expected that a decrease in measured O_2 concentration in the soil and in the efflux of CO_2 from the soil would be seen. As the soil was drained of water, gas exchange was expected to increase, resulting in higher CO_2 efflux measured and greater O_2 abundance throughout the soil column. In particular, the MuFO readings would show less O_2 under the saturated conditions than the unsaturated conditions.

In the FTC experiment, it was hypothesized that under frozen conditions, the topmost pore water would freeze when the temperature was below zero degrees centigrade. As the temperature gradient becomes established, liquid water from deeper unfrozen layers would migrate to the freezing front (Bunting, 1965). As this water freezes, expanding in volume, the air-filled pore volume through which gas diffuses would be decreased. If all of the top pore spaces are filled with ice, then a seal can form, blocking gas exchange. The measured O_2 in the soil column (unsaturated zone) was expected to decrease in sub-zero conditions with increasingly limited replenishment from the atmosphere to lower regions of the column. In addition, the emission of temperature sensitive microbial respiration products (CO_2) was expected to decrease under the lower temperature. During the thaw period, it was expected that the CO_2 efflux would increase as the ice melted from the pore spaces, reopening gas diffusion channels and as aerobic respiration restarted and microbial activity increased in response to warmer temperatures. Similarly, the O_2 levels in the unsaturated zone were predicted to increase with replenishment from the atmosphere as diffusion increased. These dynamics in O_2 levels are what we ultimately hoped to capture with the MuFO system.

The main objective of this study was to develop and test an affordable optode system capable of monitoring soil oxygen dynamics under fluctuating temperature and soil moisture conditions. Following this introduction (Chapter 1), the materials and methods for the optode design and experiments used for testing are explained (Chapter 2). The results of the

optode testing and experiments are presented in Chapter 3 and discussed in detail in Chapter 4. Finally, the conclusions drawn from this research are presented in Chapter 5.

CHAPTER 2: MATERIALS AND METHODS

In this chapter, the materials and methods used to construct the MuFO system are described following a brief review of optode theory. In addition, the materials and methods implemented in the WT experiment and the FTC experiment are presented.

2.1 Optode Theory

Optode operation is based on the quenching of luminescence. This luminescence is caused by the emission of energy when the luminophore (i.e. a chemical that is optically sensitive to the presence of an analyte) drops from an excited vibrational energy to a ground state. The luminescence is measured by light intensity (I) or by the luminescence lifetime decay (τ). For intensity measurements, when the luminophore is illuminated by an excitation light of a certain wavelength (447.5 nm in this set-up), electrons in the luminophore are excited to a higher energy level and then emit light of a given intensity as they return to a lower energy level. In the presence of an analyte, such as O_2, this emitted light intensity is diminished through collisional quenching (Figure 1).

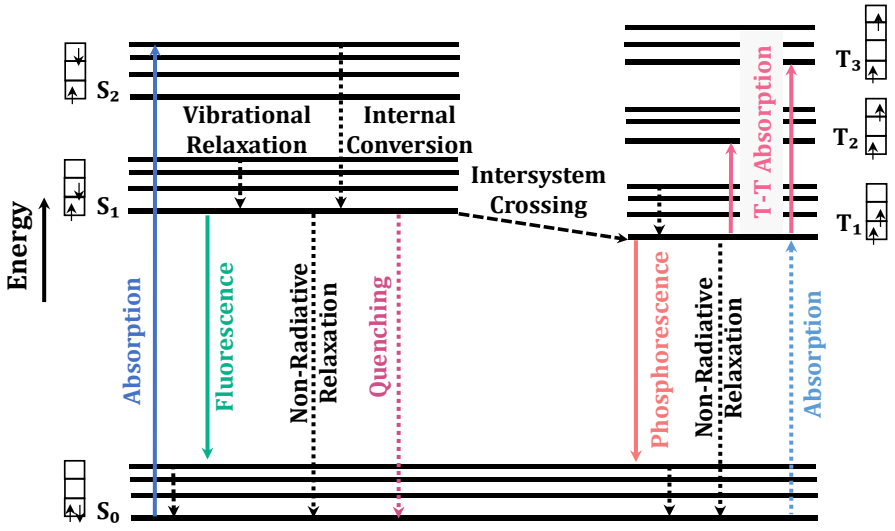

Figure 1: Jablonski diagram from Xu *et al.* (2014). S_0, S_1, and S_2 represent the luminophore in the singlet electronic state where the spins of electrons at the same energy level are opposite. T_0, T_1, T_2, and T_3 represent the luminophore in the triplet state where the electron spins are parallel. The subscripts indicate progressively higher energy levels with 0 being the lowest energy state (ground state). Vibrational relaxation and internal conversion are non-radiative decreases in energy, occurring soon after excitation. Intersystem crossing is the non-radiative process where the electrons transition from the singlet to triplet states. Further explanation follows on page 8.

Kautsky (1938) found that the degree of quenching is dependent upon the O_2 concentration in that the intensity is inversely related to the O_2 concentration, following the Stern-Volmer (SV) equation (Stern and Volmer, 1919). However, the exact relationship is unique to each sensor depending on the manufacturing process (*e.g.* resulting from variation in sensor thickness, luminophore concentration, etc…). The kinetic scheme of this process is discussed in Badocco *et al.* (2009a, 2009b, and 2012,) as:

$$M + hv \rightarrow M^* \quad k_{abs} \qquad (1)$$

$$M^* \rightarrow M + hv' \quad k_f^0 \qquad (2)$$

$$M^* \rightarrow M + heat \quad k_i \qquad (3)$$

$$M^* + O_2 \rightarrow M + O_2 \quad k_q \qquad (4)$$

where M represents the luminophore in the ground state, M^* represents the luminophore state when it is photochemically excited, hv represents the (absorbed) excitation photon energy where v is the frequency of light and h is Planck's constant, and hv' is the emitted energy, k_{abs} is the absorption rate constant, k_f^0 is the emission rate constant, and k_i is the non-radiative decay rate constant.

Equation 1 shows the photochemical excitation (shown in Figure 1 as change from S_0 to S_2 and then S_1, following internal conversion) of the luminophore while equations 2 and 3, both representing the photochemical decay, show the spontaneous (return to ground state, generating luminescence) and non-radiative (heat emission, not light) decay, respectively. Equation 4 shows the luminescence quenching by oxygen with k_q being the quenching rate constant. The visual representation of these processes can be seen in a Jablonski diagram (Figure 1). Assuming the M^* is at steady-state and that the optode membrane is made of only one luminophore and is homogeneous, the luminescence quenching process can ultimately be expressed by the classical SV equation:

$$\frac{I_0}{I} = \frac{\tau_0}{\tau} = 1 + K'_{SV}[O_2] \qquad (5)$$

where I_0 and τ_0 denote the emitted intensity and lifetime, respectively, in the absence of oxygen; I and τ are the respective intensity and lifetime in the presence of oxygen; $[O_2]$ is the concentration of oxygen present; and K'_{SV} is the SV constant, which is the product of τ_0 and k_q (Badocco *et al.*, 2012).

Equation 5 produces a linear relationship between I_0/I and $[O_2]$, also referred to as the SV plot, and is valid if dynamic/collisional quenching is the only process affecting the fluorescence measured. Deviations from the linear plot indicate the occurrence of additional processes that are unaccounted for by equation 5. As explained in the review paper by Geethanjali *et al.* (2015), an upward curvature from the linear SV plot indicates static quenching (quencher binds to or complexes with a luminophore in its ground state, decreasing the available sites for dynamic quenching), while a downward curvature can be caused by influences of inhomogeneity in the luminophore resulting in significant variations in the quenching ability of different regions of the sensor. Modification can be made to SV equation to account for both processes (Rohatgi-Mukherjee, 1978,; Lo *et al.,* 2008; Geethanjali *et al*., 2015). Downward curvature as a result of the second process was found to be the case for the sensor calibration used in the FTC experiment (see section 2.2.3). This process can be accounted for by modifying the SV relationship as shown by equation 6. This solution is a "two-site" model, which assumes that the sensing environment of the luminophore has two regions with significantly different accessibility to oxygen affecting the luminescence emission, and is used to correct for microheterogeneities in the optode (Quaranta *et al.*, 2012):

$$\frac{I}{I_0} = \frac{f_1}{1+K_{SV_1}[O_2]} + \frac{f_2}{1+K_{SV_2}[O_2]} \qquad (6)$$

where f_1 and f_2, represent the primary quenchable fraction and the smaller, "unquenchable" (inaccessible) fraction of the luminophore for the sensor, respectively, and the Ksv_i values show the sensitivity of each site to oxygen. Note that the sum of f_1 and f_2 amounts to 1. For simplicity it is often assumed that $Ksv_2 = 0$, hence the equation can be rearranged and rewritten to give equation 7.

$$\frac{I_0}{\Delta I} = \frac{1}{1-f_2} + \frac{1}{f_1 K'_{SV}[O_2]} \qquad (7)$$

where *ΔI = Io - I*. This can further be rewritten as equation 8, also referred to as the Lehrer equation in Geethanjali *et al.* (2015):

$$\frac{I_0}{\Delta I} = \frac{1}{f} + \frac{1}{f K'_{SV}[O_2]} \qquad (8)$$

Equation 8 is used for calibration of the optode sensors for the FTC experiment because the calibrations curves for the FTC showed a downward sloping deviation from the SV relationship. Equation 5 is used in the WT fluctuation experiment because the calibrations curves were all linear. This is further explained in section 2.2.3.

2.1.1 Interference

Wang and Wolfbeis (2014) summarize a variety of factors that, in addition to oxygen, can influence the luminophore intensity measured. These include certain heavy metals, some ionic species (if they can pass through the optode matrix), elemental chlorine and bromine, relative humidity (as it affects diffusion of oxygen through the matrix), some organic solvents (which might degrade the matrix), and temperature. Each of these effects can be minimized by sensor design and application methods. For the purposes of this research, temperature was the main effect of concern for the FTC experiment, while the change in moisture content was the main focus of the WT experiment. In the FTC experiment, effort was made to keep the humidity levels constant (section 2.4) while the temperature fluctuated. In the WT experiment, the temperature was constant (room temperature, see section 2.6) and the soil moisture fluctuated. Since heavy metals, and elemental chlorine and bromine were not included in the pore water composition or detected in the soil composition, any effect from these influences was not considered.

Optodes are known to be sensitive to temperature (regardless of whether the measurement is in terms of intensity or lifetime), which affects gas solubility, diffusion, and permeability in the matrix as well as the quantum yield (ratio between number of photons emitted to number of photons absorbed (Lakowicz, 1999)), luminescence lifetime, and the quenching

rate constant of the luminophore, all converging to make the temperature dependence most difficult to quantify. More specifically, increasing temperature will increase *K'sv* values and oxygen diffusion in the sensing membrane, while decreasing the sensor response time, quantum yield of the luminophore, and the solubility of oxygen in the membrane (Wang and Wolfbeis, 2014).

Various solutions have been proposed for the temperature correction. Lo *et al.* (2012) applied a correction factor, *C(T)*, to the raw intensity values to report the intensities relative to a reference temperature. Kocinova *et al.* (2007) used the addition of another luminophore, ruthenium (II), to directly monitor temperature at the sensing point for which a correction could subsequently be applied. Badocco *et al.* (2012) used the Arrhenius equation to address the solubility, luminescent lifetime and diffusion of oxygen in the sensing membrane in the range between 40 °C and 90 °C. Bagshaw *et al.* (2011) and Mock *et al.* (2002) both used PreSens optodes (with pre-set salinity and temperature corrections) to measure dissolved oxygen in water down to -5 °C and -10 °C, respectively. However, to date, no sub-zero temperature dependence has been investigated in a variably saturated soil environment (based on review by Santner *et al.*, 2015). This is a much needed area for investigation and is also what makes this research, with the particular freeze-thaw application, unique. The temperature dependence of the MuFO sensor here was determined by repeating a calibration at progressively lower temperatures as shown in section 2.3.1 and applying the final reference calibration to all temperatures following the approach proposed by Lo *et al.* (2012).

2.2 Multi-Fibre Optode System

The optode system used in this study is based on the quenching of luminescence intensity of a luminophore that is imbedded in a polymer matrix. The luminophore-matrix solution is coated onto the tips of fibre optic cables, which function as waveguides for light (both excitation light and emitted luminescence). The use of fibre optic cables is appealing because it allows for *in-situ* measurements at the user designed spatial distribution.

As mentioned in section 2.1, the change in luminescence can be detected by measuring light intensity or the luminescence lifetime decay. Detection schemes based on luminescent lifetime (a property intensive to the luminophore) are viewed as superior in resisting signal drift and interference. This is because, unlike the luminescence intensity-based measurements, luminescent lifetime is not influenced by factors such as photobleaching, the homogeneity of the excitation light or the homogeneity of the sensing membrane and luminophore distribution, (Wang and Wolfbeis, 2014). However, the lifetime measurements are more complex and expensive to obtain, particularly for imaging systems (Santner et al, 2015) compared to direct light intensity methods, which are simple in design and low in cost (Badocco *et al.*, 2012, 2013b; Santner *et al.*, 2015). Thus, intensity measurement was the chosen approach.

In addition to the sensors and excitation light source, the optode system has an interrogation component, which is the instrumentation for data collection. Here the interrogation method was digital imaging using a camera and subsequent image processing for analysis of the photographed light intensity. The system is further discussed in detail below. A schematic diagram of the O_2 fibre optode system is shown in Figure 2. This MuFO set-up currently allows for 16 sensors (each monitoring 0.78 mm^2) to be used simultaneously in any arrangement. This way a total of 12.57 mm^2 can be monitored.

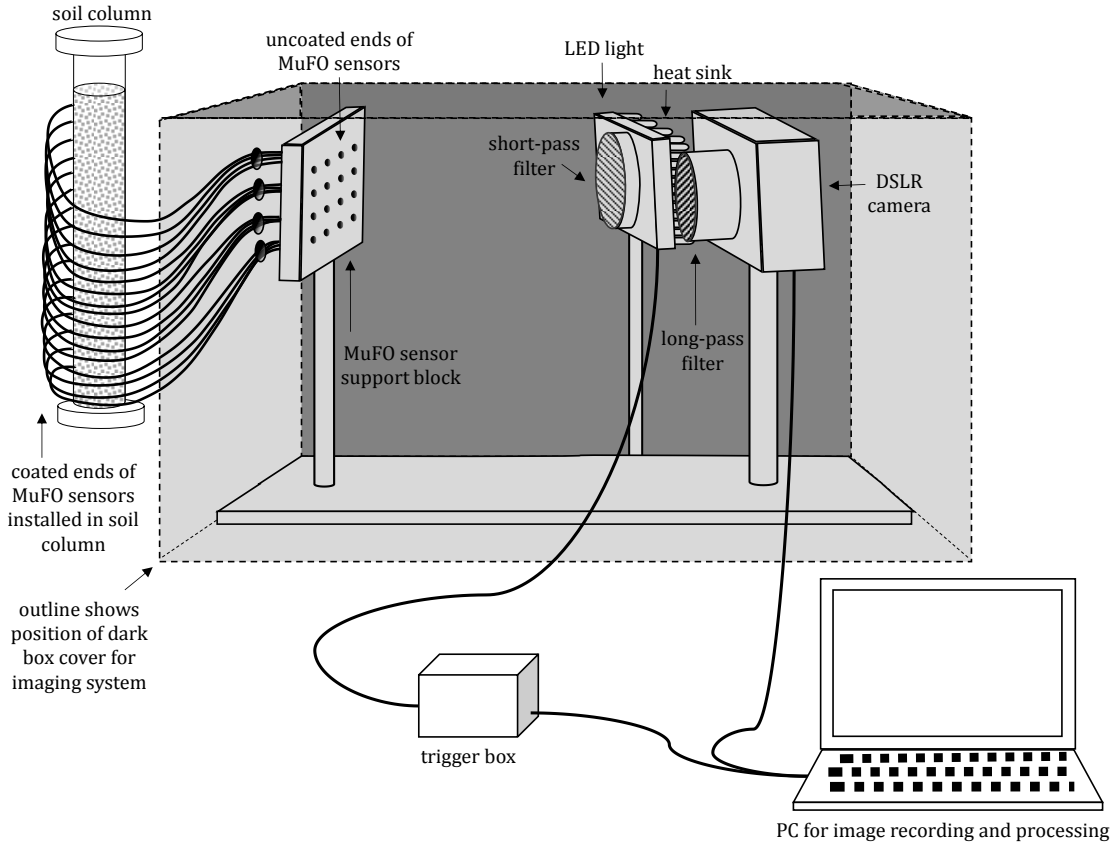

Figure 2: Schematic diagram of the oxygen fibre optode microsensor system. The LED providing excitation light shines on the uncoated tips of the fibre optic cable, which is the waveguide directing the light to the PtTFPP coated tips in the sample. The fluorescent light emitted travels back down the cables and is photographed at the uncoated end by a DSLR camera. The photographs are stored on a PC and later the light intensity is analyzed by digital signal image processing and converted into and oxygen reading. Coordination of the LED light and camera is controlled by a trigger box.

2.2.1 Sensors

The sensing mixture selected for use in this method is from Badocco *et al*. (2012, 2013a, 2013b), who researched and characterized the formula based on light intensity measurements. The method was initially chosen because of the reported linearity when calibrated and the simplicity in the manufacturing processes. The optode was created following the protocol in Badocco *et al.* (2012); the solution was made by dissolving 11.8 mg of Pt(II) meso-Tetra(pentafluorophenyl)porphine (PtTFPP) (from Frontier Scientific; see Figure 3), which was the luminophore, and 75.5 mg of polysulfone (PSU) (average Mn ~22,000 by MO, beads from Sigma-Aldrich; see Figure 4), which was the matrix for the luminophore, in 1 mL of chloroform (anhydrous, ≥99 %, contains 0.5-1.0 % ethanol as

stabilizer, from Sigma-Aldrich). The resulting optode solution was coated onto fibre optic cables. Each sensor consisted of 1.5 m length of fibre optic cable with diameter of 1 mm (from Edmund Optics, #02-536), that was cut using a Fibre Optic Cutting Block (Edmund Optics, #54-013) to ensure the smoothest surfaces possible. One end of each cable was manually dipped into the optode solution and then removed slowly to ensure that the solution coated the entire cable core surface. Next, the cable was inverted and secured in a vertical position so that the coating would dry flat.[1] The tips where left to dry in a dark room for about 24 hours at room temperature (23 °C ± 1 °C). Once dry, the sensors were calibrated then manually installed at different depths in the soil experiment columns.

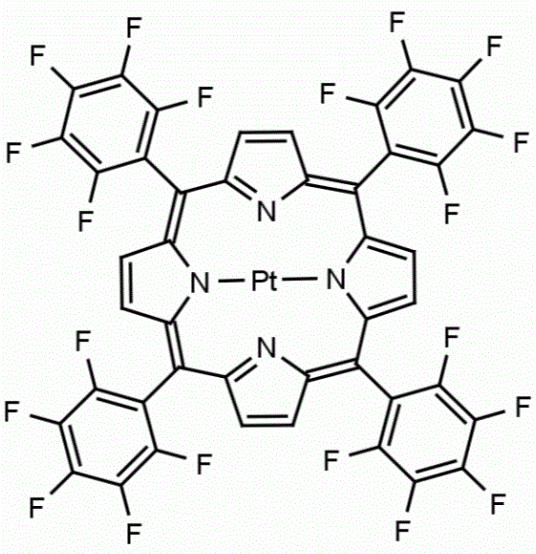

Figure 3: Pt(II) meso-Tetra(pentafluorophenyl)porphine structure image from Frontier Scientific (catalogue product number PtT975).

PtTFPP is a popular luminophore because it has a large Stokes' shift, good quantum yield, comparatively low temperature sensitivity, and good resistance to photobleaching (Wang and Wolfbeis, 2014). The larger Stokes' shift means that the difference between the excitation and emission wavelengths is large enough that the light can be separated well by optical filters, validating the MuFO light interrogation set-up. The quantum yield describes

[1] It should be noted that the sensors used in these experiments were made under an atmosphere of air, which may diminish the collisional quenching ability (i.e. lower f_1 value) if any O_2 bubble is trapped in the matrix. This could decrease the sensitivity of the sensor since oxygen is already incorporated in the film. Therefore, future sensors should be made under an N_2 or other anoxic environment if possible. A glove box can be used for this where available.

the emission capacity of the luminophore by the ratio between the number of photons emitted to the number of photons absorbed. PtTFPP has a high quantum yield, ideal for optode systems (Wang and Wolfbeis, 2014). Lower temperature sensitivity is important, particularly where temperature fluctuations are expected to occur, such as in the freeze-thaw experiment. Finally, resistance to photobleaching is ideal because photobleaching is known to degrade the luminescence response of sensors over time. This is important for long term experiments and/or where frequent measurements (i.e. frequent light excitation) are required.

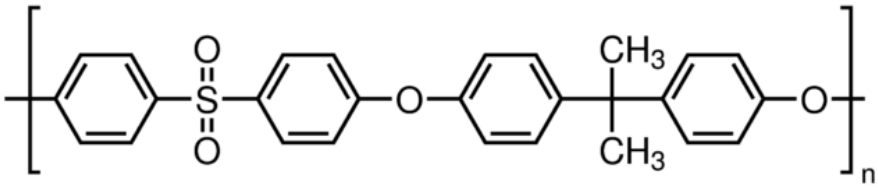

Figure 4: Polysulfone structure image from Sigma-Aldrich (catalogue product number 25135-51-7).

PtTFPP is compatible with PSU, which is used as the matrix support in this optode (Badocco *et al.*, 2012). PSU is a thermoplastic polymer that maintains its rigidity, strength, and optical properties over a temperature range of -100 °C to +150 °C (Diogo and Ramos, 2012). This makes it a good choice for use as a matrix for optodes deployed in dynamic temperature conditions over the stated range, such as the freeze-thaw experiment presented here.

2.2.2 Imaging

The interrogation method follows a similar design to that by Larsen *et al*. (2011). This design was chosen because of the simplicity and low cost (quoted at $3,000 USD by Larsen *et al*. (2011)). The uncoated ends of the cables were placed in a support block (Figure 2), secured in the focal plane in front of a digital single lens reflex (DSLR) camera (Canon EOS Rebel T3). The camera was mounted on a metal stand and connected to a computer via USB. A Royal-Blue (447.5 nm) LUXEON Rebel LED (light excitation source for PtTFPP), mounted on a 40 mm Round 7-Up CoolBase, 6370 mW at 700 mA (Luxeon Star LEDs), was fitted to a custom-made stand that was set as close as possible to the camera (to minimize space). The uncoated cable tips, camera, and LED were enclosed in a custom-built housing (see Figure 2) to

prevent ambient light interference. A trigger box was used to coordinate the imaging by the camera with the LED (850 mV) light pulse (Larsen *et al*., 2011). This way the LED light was only on when an image was taken by the camera. Thus, while the phosphorescent decay time of Pt(II) porphyrins varies between 40 to 80 µs (Quaranta *et al.*, 2012), in this MuFO design the temporal resolution is actually determined by the trigger box setting, which is able to coordinate the LED pulse and digital camera to a minimum time of 2 seconds between each reading (imaging each photo). Despite the high temporal frequency capability of imaging every 2 seconds, imaging was limited to 60 minutes between readings in the experiments presented here. This was done to reduce light exposure time to limit photobleaching effects, which degrade the optode over time (Wang and Wolfbeis, 2014) and limit excess heat generation from the LED. The trigger box was connected to both the LED light and the computer and it was controlled using the corresponding Look@RGB software. Details of both the trigger box (hardware) and Look@RGB software can be found in Larsen *et al*. (2011).

The images were saved in the Canon RAW version 2 (CR2) format and then converted into an RGB colour, tagged image file format (tiff) using the Canon "Digital Photo Professional" software. These tiff files were then opened as stacks (an organized collection of the images, used for executing the same action on every image with one command) within ImageJ software (Rasband, 2005) and subsequently converted into 8-bit format. Within ImageJ, an ROI (region of interest) file was made in order to select the desired areas (example in Appendix A1) for light intensity measurement from each image in the stack. This way the average light intensity was found for each sensor area. The mean of the duplicate images (values typically within 0.6 % of each other at both high and low O_2 saturations) at each hour of each experiment was calculated and taken as the final light intensity value for that time. This intensity was later converted into a percentage of O_2 saturation (relative to atmospheric O_2 % saturation) value based on the calibration data and SV equation.

2.2.3 Oxygen Optode Calibration

The MuFO sensors were calibrated prior to the experiments. For the freeze-thaw experiment, the calibration was conducted in a similar setting to the actual experiment. A soil column composed of the same porous media mixture as used in the experiments was

placed in an environmental chamber where temperature could be controlled. Seven MuFO sensors were installed at various depths along the soil column (although, only the calibration curve from the sensor located at -3 cm from the soil surface was used in the end; see Appendix A2). Then the lower part of the column was saturated with deoxygenated water, to facilitate the development of an anoxic region. This is reasonable because the half saturation constant for aerobic respiration is 0.1 mg L^{-1} (Moyer and Kostecki, 2003), so it would be expected that the O_2 concentration in the lower, saturated region of the soil would rapidly drop below 0.1 mg L^{-1} as any O_2 is preferentially used prior to alternative terminal electron acceptors by the microbial community (Wang and Van Cappellen, 1996).

Nitrogen (N_2) and air gas lines were connected in the headspace of the column to allow transition between anoxic and oxic conditions at the surface of the soil, respectively. The headspace of the column was first purged with N_2 gas to establish anoxic conditions in the soil column. The O_2 saturation in the headspace was measured using an Orion 5 Star dissolved oxygen (DO) probe from Thermo Scientific (resolution 0.1 %, relative accuracy ±2 %, for specified temperatures of -5 °C to 105 °C). Once the DO probe reached a stable value (<0.1 % change in 5 minutes), the gas line was switched from N_2 to air and left to flow into the column until the DO probe reading stabilized at a maximum value (90-100 %). Calibrations were conducted at temperatures of 25 °C, 15 °C, 10 °C, 5 °C, 0 °C, -5 °C and -10 °C for a total of seven runs. The calibration soil column was left overnight (~12 hours) to equilibrate at each temperature prior to the trials being conducted to allow for uniform soil temperature throughout the column.

The DO probe readings were directly correlated to the light intensity readings as measured by the MuFO sensors. Unfortunately, no other oxygen meters or gas mixers were available for additional measurement to verify the DO readings for the calibration. Thus, the DO readings were directly used as the $\%O_2$ values related to each intensity value, the uncertainty from the DO probe is passed on to subsequent optode readings. Future calibrations should be verified using additional oxygen measurements or controls. For instance a gas mixer and analyzer can be used to control the oxygen amount and monitor the content in addition to the DO probe.

Luminescence based O_2 sensors are normally calibrated and converted into an O_2 concentration from intensity (or luminescent lifetime) on the basis of the SV equation (Santner *et al.*, 2015). The luminophore mixture used here was initially chosen due to good reported linearity, however, the calibration curve produced was not linear for every sensor. The deviation from linearity in the calibration for the freeze-thaw experiment at various temperatures is shown in Figure 5.

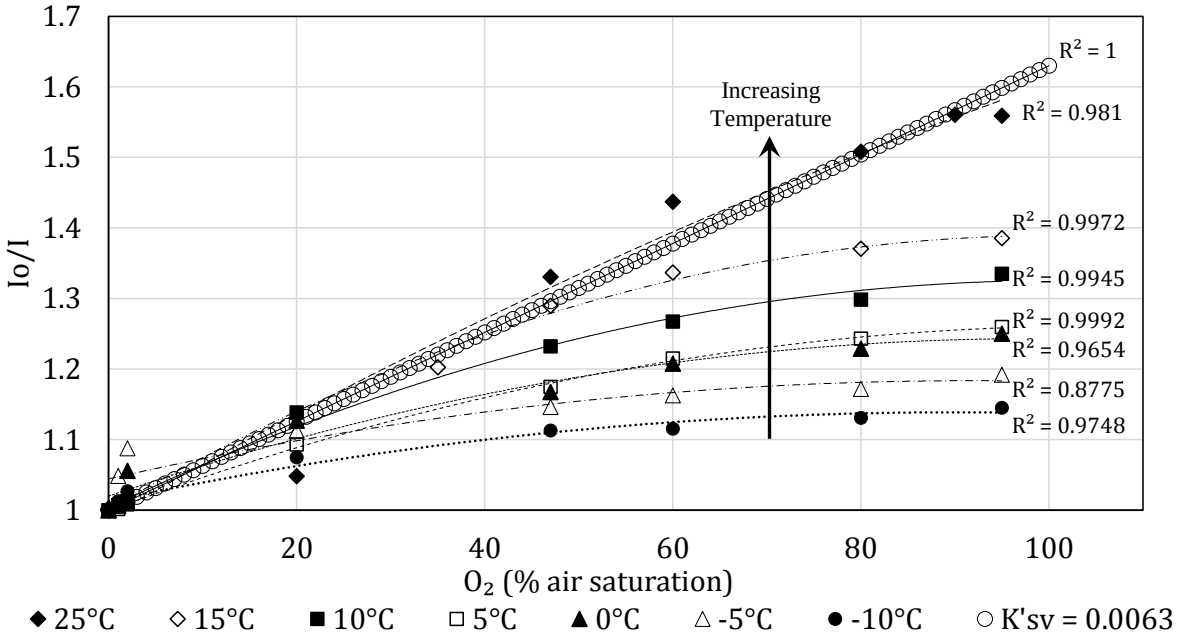

Figure 5: Deviation of sensor freeze-thaw calibration data at various temperatures (-10 °C to +25 °C) using *Io* = 95.302 (i.e. correct to Io at 10 °C, compared to theoretical linear SV equation based on *K'sv* = 0.006 (i.e. *pK'sv* = 2.2).

Here the curves all slope downwards relative to the linear SV plot for a *K'sv* of 0.006, indicating the probable presence of inhomogeneities in the sensing matrix, as explained in Section 2.1 on optode theory. Thus, a modified SV equation (from Lo *et al.*, 2008) was applied in the form:

$$O_2\% = \frac{I_{O(Tref)} - I_m \times C(T)}{\left[\left(I_{O(Tref)} \times (f(T) - 1) + I_m \times C(T)\right) \times K'sv_{(Tref)}\right]} \qquad (9)$$

This equation is in fact the Lehrer equation (to correct for the non-linearity) with an added temperature correction factor (to compensate for the temperature fluctuations). $I_{O(Tref)}$ is

the intensity in the absence of oxygen, calculated at a reference temperature of 10 °C to be 95.302 arbitrary unit (a.u.) values (extending from 0, which is the absence of light to 255, which is the highest measureable light intensity); I_m is the intensity measured at temperature (T in °C); and $K'sv_{(Tref)}$ is the SV constant calculated from the calibration at 10 °C. $f(T)$ represents the quenchable fraction of the sensor at temperature (T) and follows the relationship:

$$f(T) = 0.0076 \times T + 0.2825 \qquad (10)$$

This relationship was obtained by applying the Lehrer equation (equation 8) to the data at each calibration temperature (see Figure 6), where the intercept was equal to $\frac{1}{f}$ and the slope was represented by $\frac{1}{(f \times K'sv)}$.

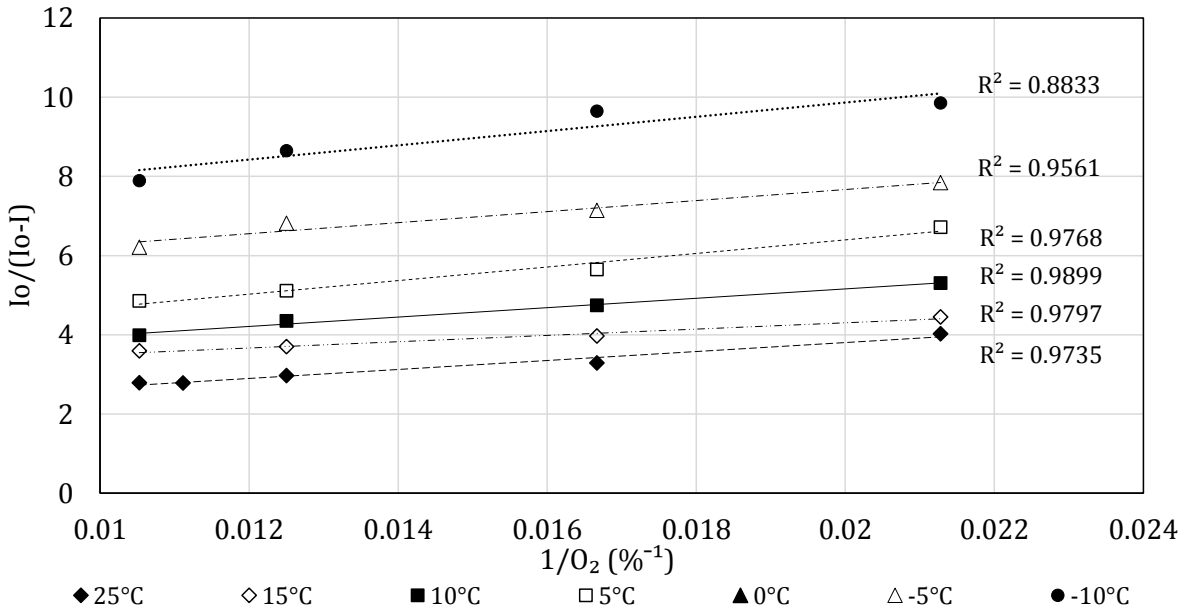

Figure 6: SV plot (based on Lehrer equation) of calibration data points taken a various temperatures.

The coefficient, $C(T)$, in equation 9 is the temperature correction applied to the measured intensity I_m at T and is calculated based on each calibration temperature curve as:

$$C(T) = \frac{I_{O(Tref)}}{I_m} - \frac{I_{O(Tref)} \times f \times K'sv \times [O_2\%]}{I_m(1+K'sv \times [O_2\%])} \qquad (11)$$

The average values from the temperature calibration where plotted against temperature (Figure 7) to give the *C(T)* relationship that was applied to the freeze-thaw experiment data:

$$C(T) = 0.0046 \times T + 0.9946 \qquad (12)$$

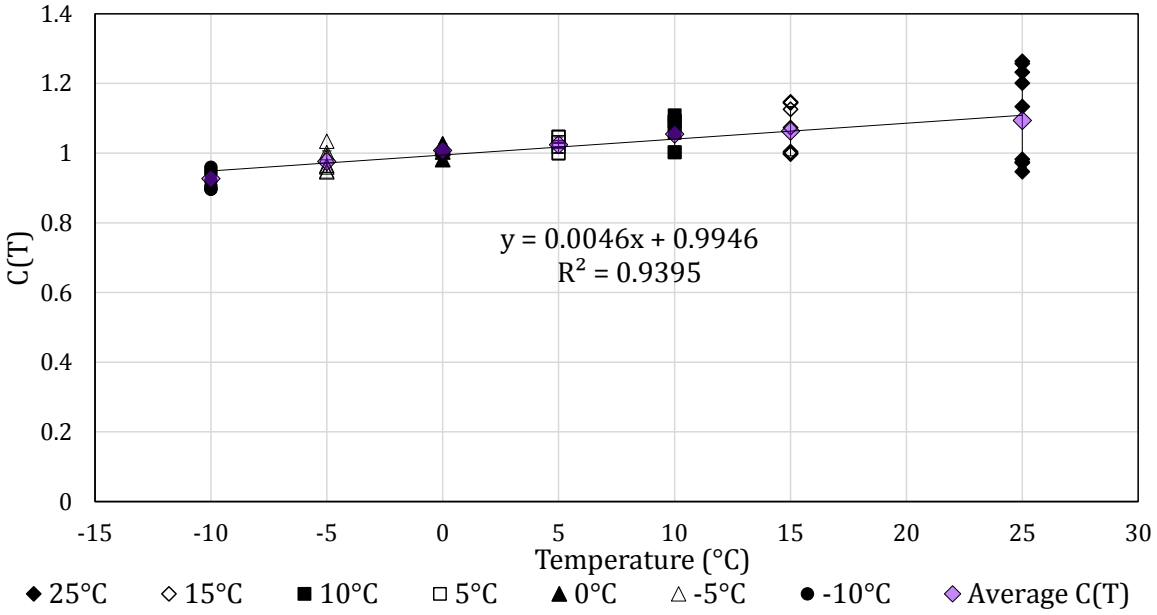

Figure 7: Plot of temperature correction coefficient, *C(T),* varies in temperature. The vertical spread of *C(T)* values at each temperature correspond to an oxygen (% saturation) value ranging from 0 % to 100 %. The average value is calculated at each temperature based on the *C(T)* values across that oxygen range. Note that the higher temperatures have a larger *C(T)* range because they have a larger range on intensity values (I_o to I).

The correction was reapplied to the calibration data (from Figure 6) to verify that it indeed worked as intended (see Figure 8).

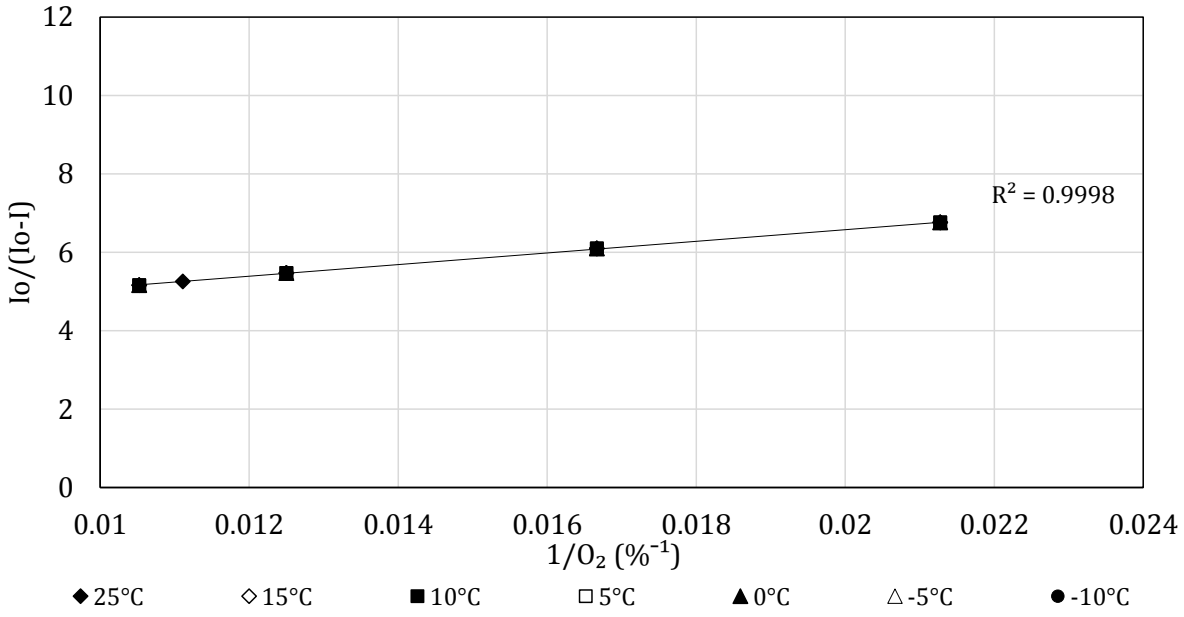

Figure 8: SV plot (based on modified SV equation) of calibration data points at various temperatures after applying the temperature correction factor *C(T)*; in comparison to Figure 6, shows all values are now on same line. All symbols are present, but may not be visible due to overlapping values.

These data set came from the calibration sensor at -3 cm in the calibration soil column and was one of the few (three sensors in total) sensors to show a clear response and complete plot of O_2 data for the full range of temperature calibrations from 25 °C to -10 °C. Thus, while additional repeated cycles would have been beneficial in improving the confidence in this relationship, this one data set, which showed the clearest response, was used for calibration in all of the sensors used in the freeze-thaw experiment. This worked well, however, it was ultimately determined that since the optode sensors are made individually using this method it is best to calibrate each sensor separately for future measurements.

Unlike the FTC sensor calibrations, the calibrations for the sensors used in the WT experiment were done individually for each sensor in water-saturated air. These calibrations showed a linear relationship (R^2 values in Table 1) between the oxygen levels and the *Io/I* (ratio between emitted light intensity in the absence of oxygen to the intensity in the presence of oxygen). Therefore, the unmodified SV equation (equation 5) was used to convert the light intensity data into an oxygen level (% relative to saturation of air) for the WT experiment. The *K'sv* values and the *Io* values used for the sensor at each monitored depth are shown in Table 1, which corresponds to the room temperature of 23 ±1 °C.

Depth (cm)	-3.5	-6.5	-9.5	-12.5	-18.5	-21.5	-24.5	-27.5
Io	121.93	127.28	69.248	125.1	130.04	160.21	87.32	139.09
K'sv	0.0014	0.0027	0.0035	0.0039	0.0037	0.0008	0.0067	0.0011
pK'sv	2.9	2.6	2.5	2.4	2.4	3.1	2.2	3.0
R^2	0.9813	0.9864	0.9938	0.9915	0.9926	0.9614	0.9195	0.9892

Table 1: I_o, *K'sv*, and *pK'sv* (= - log (*K'sv*)) values obtained from calibration (conducted at room temperature and 100% humidity) curves for sensors used at each soil depth in WT experiment. R^2 values showing good linearity of the calibration curves validate the use of the classical SV equation as opposed to the Lehrer equation.

A frequent consideration in temperature corrections, in addition to the effects on oxygen concentration and membrane performance, is the effect of temperature on the electronic components. While the temperature was not monitored inside of the box where the light was measured, it is assumed that there was no significant change in the temperature resulting from the LED operation. This is a valid assumption because the trigger box allowed for the LED to be turned off when not in use during measurement, thus limiting light exposure of the sensors and limiting heat generation. In this case, as the electronics (trigger box, computer, and digital camera) were always at room temperature, there was no change in the functioning of the interrogation system so no correction was necessary.

In addition to temperature, gaseous oxygen levels are affected by humidity and, for dissolved oxygen, also salinity (Wang and Wolfbeis, 2014; Mock *et al.*, 2002). As the humidity increases, oxygen molecules are displaced and will decrease in absolute amount. In soils, the humidity is assumed to be 100 % as justified in other soil oxygen studies (*e.g.* Haberer *et al.*, 2011). Given this assumption, it can be expected that the partial pressures of O_2 dissolved in water and O_2 in the air-filled pore-space are in equilibrium, following Henry's law (Haberer *et al.*, 2011). While humidity was not measured during the experiments, the headspace of the FTC soil column was flushed with humid air to limit changes in soil moisture, so no additional correction was applied in this case.

Likewise, an increase in salinity would lead to less dissolved oxygen. For instance, when salinity increases from 0 µS cm^{-1} to 1000 µS cm^{-1}, the salinity correction factor for dissolved oxygen in water at temperatures ranging from 0 °C to 10 °C changes from a value of 1.000 to 0.996 (Rounds *et al.*, 2013). Thus, since the pore water electrical conductivity was on

average, 0.8 mS cm^{-1} (Appendix A3) throughout the freeze-thaw experiment, across the column, and under both frozen and thawed conditions, no correction factor was applied for salinity. This same pore water composition and soil mixture was used in the WT experiment, so the EC data is considered representative of both cases.

2.4 Experimental Set-Up

The experimental set-up for the WT and FTC experiments are shown in Figure 9. Soil systems are a multi-phase systems consisting of the air-filled pore-space for gases, liquid water-filled pore-space, soil particles, and, for the freeze-thaw column, the solid phase consisting of ice (Beneš *et al.*, 2015). The ratios between these phases change depending on the location of the water table level (for WT) and on the temperature (for FTC) at a given time. Assuming no evaporative losses, the amount of water (liquid and ice) would be constant.

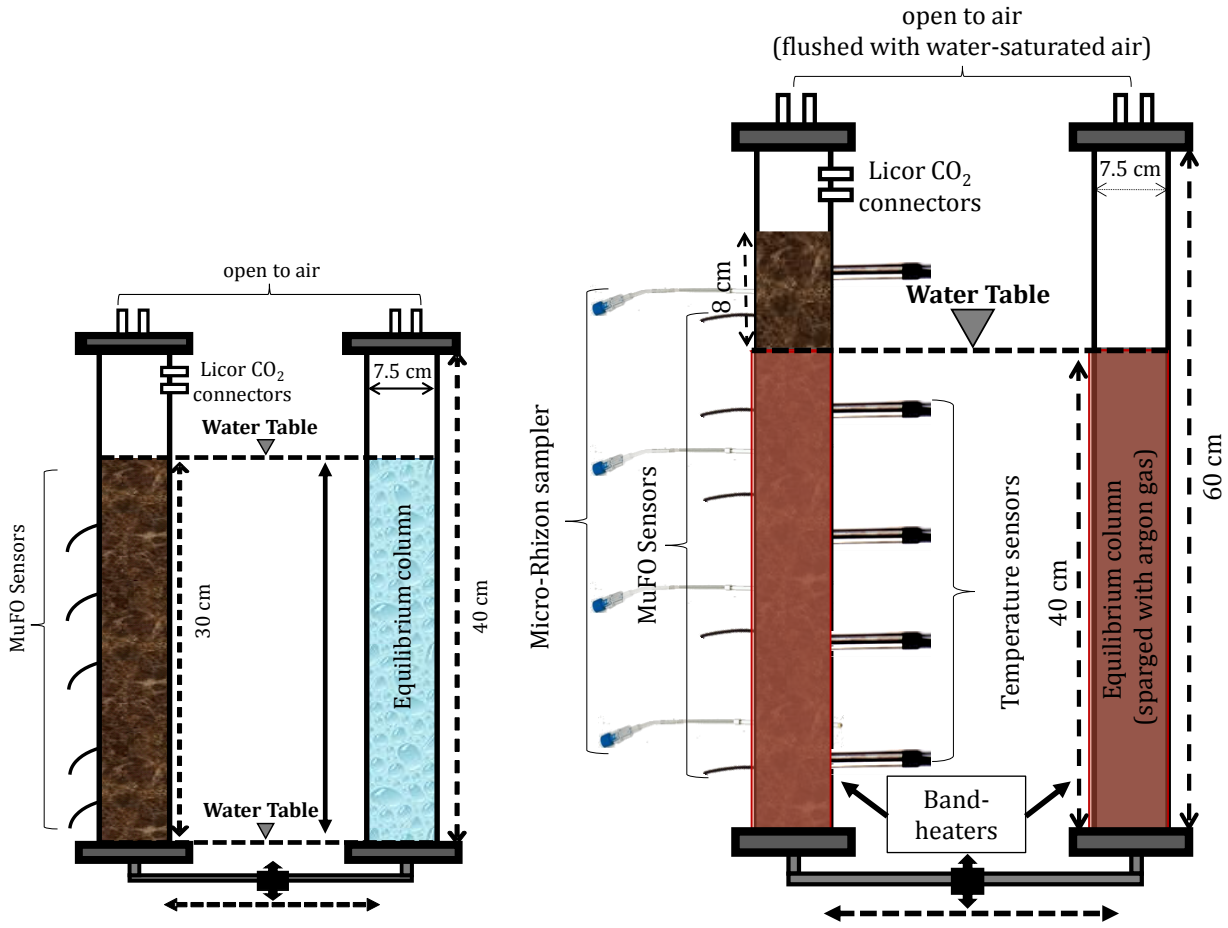

Figure 9: Schematic diagram of the WT fluctuating (left) and FTC soil column (right) set-up.

In the WT experiment, a soil column system was used to simulate water table fluctuations to generate a dynamic range of oxygen levels along the soil depth. The height of the water table in the soil column was imposed using a hydrostatic equilibrium reservoir. This equilibrium column was used to set the position of the water level in the soil column, while the water was supplied slowly to the equilibrium column during water table rise and drained during drawdown by a peristaltic pump. The soil column and auxiliary equilibrium column casings were made of hard acrylic with dimensions matching the soil cores of 7.5 cm inner diameter and 40 cm length (see Figure 10). The two columns were connected to one another with chemically resistant polyurethane tubing. Further details on the column systems can be found in Rezanezhad *et al.* (2014).

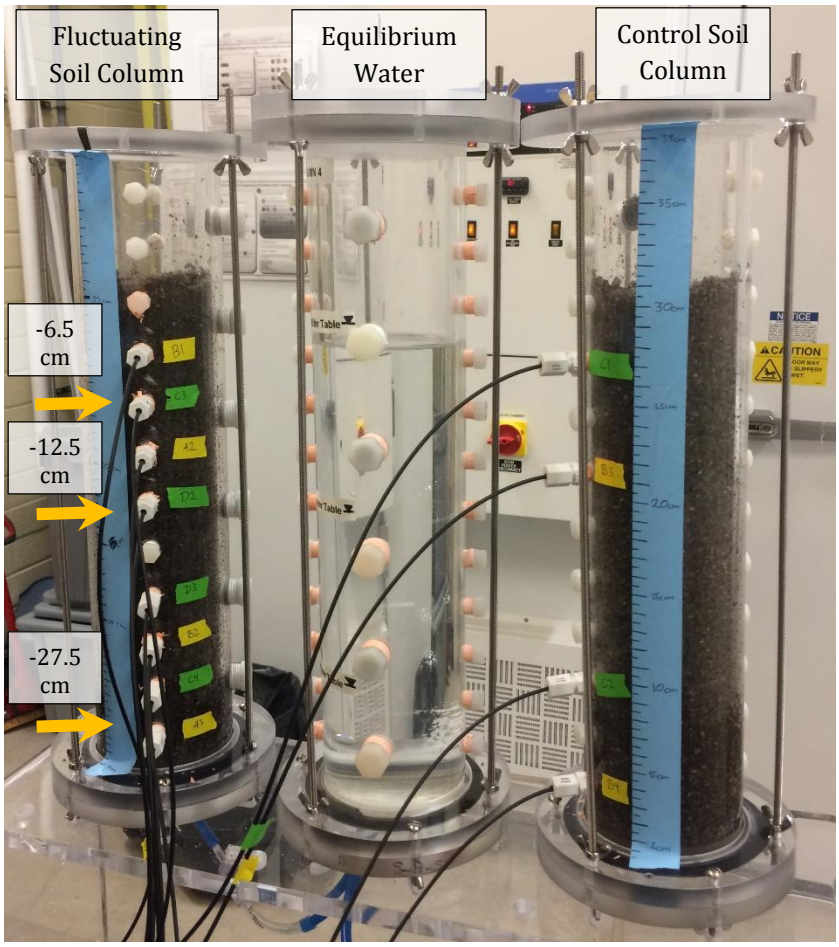

Figure 10: Photograph of soil column from WT experiment set-up. Displayed are the equilibrium water column, the fluctuating soil column, and the control soil column. Note that the columns were covered in aluminum foil during the actual experiment to block ambient light that might interfere with the sensors and stimulate algal growth and other photochemical processes.

For the FTC experiment, a novel instrumented soil column system (Figure 11) was used. This system allowed implementation of a large range of temperature (across 20 °C) to test the MuFO system performance. The equilibrium column described above was used to set the position of the water level in the soil column by hydrostatic equilibrium. The columns were placed in an environmental chamber (Percival I-41NL XC9) allowing for air temperature control. The temperature at the soil surface was set by the chamber temperature; while a 40 cm long silicone rubber band-heater (120V, 2 watts per square inch, custom-built by Gordo Sales Inc., part# 110145A1) surrounding the lower 37 cm of the soil and equilibrium columns kept the lower part of the columns at a constant temperature near to that of local groundwater at the soil sampling site (Niederkorn, 2015). The temperature was set using a control system connected to the band heaters. As the air temperature dropped below 0 °C, freezing would progress downwards from the surface of the soil. As the air temperature returned above 0 °C, the upper soil layer would thaw. Thus, the system allows one to simulate seasonal FTCs with realistic subsurface soil temperature gradients (Figure 11). Six temperature sensors (DaqLink Fourier Systems Ltd., #DBSA720) were installed, one in the chamber to monitor the air temperature and five in the soil column at depths of -3, -9, -27 and -39 cm relative to the soil surface to monitor the subsurface temperature gradients.

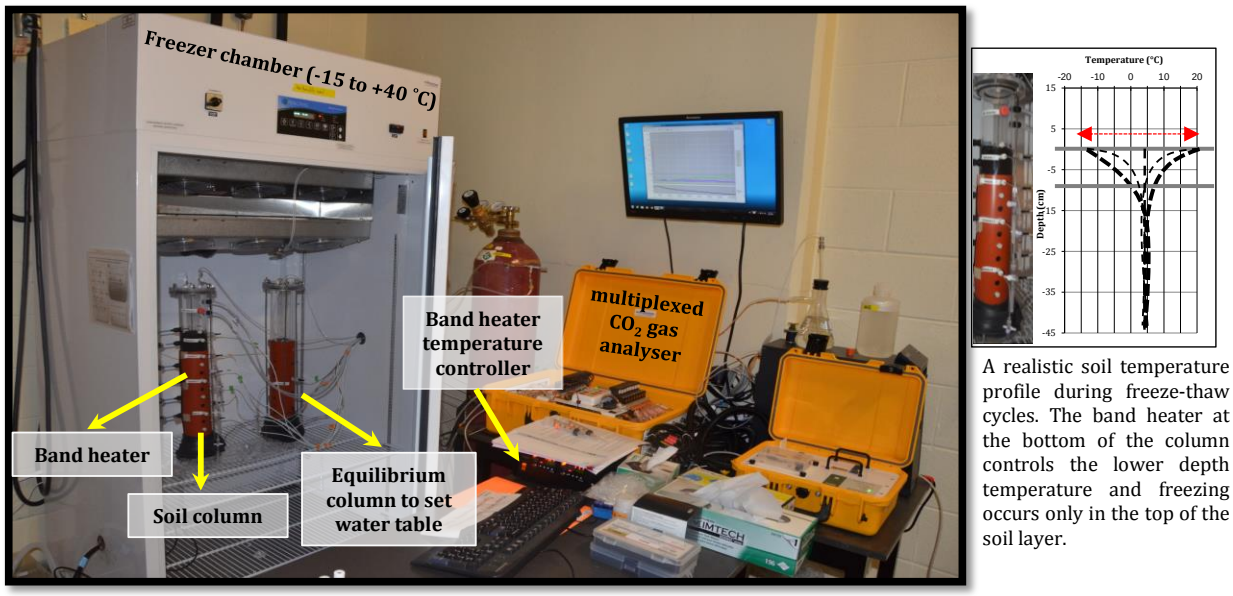

A realistic soil temperature profile during freeze-thaw cycles. The band heater at the bottom of the column controls the lower depth temperature and freezing occurs only in the top of the soil layer.

Figure 11: FTC soil column system.

The MuFO sensors were inserted at depths of -6.5, -9.5, -12.5, -18.5 and -21.5 cm in the WT soil column, and at -1, -7, -10, -16, -28 and -40 cm depths in the FTC soil column to measure real-time O_2 concentrations in the soil. The headspace of the soil columns was flushed with humid air to minimize evaporative losses through the upper ports of the columns. The headspace above the soil surface was periodically closed in order to measure the build-up of CO_2 to derive the gas efflux from the soil (see section 2.7). The soil column was saturated by upward flow of artificial groundwater (AGW), which was composed of $Ca(NO_3)_2 \cdot 4H_2O$ (0.15 mM), $CaCl_2 \cdot 2H_2O$ (1.6 mM), $NaHCO_3$ (0.35 mM), $KHCO_3$ (0.02 mM), $CaSO_4 \cdot 2H_2O$ (0.2 mM), and $MgCl_2$ (1.15 mM). This water composition was developed based on the groundwater composition (Niederkorn, 2015) from the field site where the peat soil (see section 2.5) used in the columns was collected. The equilibrium columns holding the artificial groundwater were sparged continuously with argon gas to maintain anoxic AGW. Water samples were collected from the freeze-thaw column every 1-3 days at depths of -4 cm, -13 cm, -25 cm,-35 cm, and from the equilibrium water column (input solution). These samples were used to measure pH and electrical conductivity (EC), using Spectrum Technologies LAQUA Twin pH Meter (accuracy ±0.1 pH) and LAQUA Twin EC Meter (accuracy ±2 %), respectively. The results of the EC and pH values can be found in the Appendix (A3 and A4). In an effort to preserve constant water content, any water collected during sampling was replenished by adding more of the input AGW solution (the same volume as sampled) to the equilibrium column at the end of the sample collection.

2.5 Soil Mixture and Column Packing

The soil used in each of the soil columns consisted of a mixture of 20 % moderately decomposed peat and 80 % quartz sand (20:80 by volume). The peat soil was collected at the *rare* Charitable Research Reserve (www.raresites.org) located in Cambridge, Ontario, Canada (43°22'39.80"N, 80°22'07.28"W). Samples of the soil were freeze-dried and the total organic carbon concentrations (C_{org}) were measured on a CHNS Carbo Erba analyzer. The soil was comprised of 30.9 % organic carbon content by dry weight. The quartz sand (grain size 1-2 mm, sourced from U.S. Silica sand supplier) was manually homogenized with the peat prior to packing the soil columns. This mixture was chosen to allow for good hydraulic

conductivity, while providing organic matter as an electron donor to allow for a range of potential CO_2 production in the columns. The soil columns for the WT and FTC experiments were filled with 30 cm and 52 cm of the peat-sand mixture, respectively. This left a headspace of 456 cm^3 in the WT soil column and 547 cm^3 in the FTC soil column. All depths are referenced with respect to the soil surface.

2.6 Water Table and Temperature Regimes

The level of the water table in the fluctuating soil column was varied between 15 cm above and below the depth of -15 cm (*i.e.* 0 cm to -30 cm) at the rate of 30 cm per 60 hours (2.5 days). Thus, the rising of the water level to 0 cm from the depth of -30 cm was performed over 60 hours and then the column was drained again within 60 hours to reach -30 cm depth below the soil surface. Four saturation-drainage cycles were imposed resulting in a total experimental duration of 20 days. The set flow rate in the upward and downward direction was 0.78 ml min^{-1}, which translates to a linear rate of 12 cm d^{-1}. The experiment ran at room temperature (23 ± 1 ˚C).

Six FTCs were imposed in the freeze-thaw soil column experiment, resulting in a total experimental duration of 39 days. The cycles consisted of 3 days at 10 ˚C (thawing phase) followed by 3 days at -10 ˚C (freezing phase), while groundwater temperature was kept constant at +10 ˚C. The temperature at the soil surface of the column was set by the chamber temperature and was recorded every 30 minutes during the experiment. The water level in the freeze-thaw soil column was kept at -8 cm below the soil surface. The water table and the freeze-thaw regimes were selected to test the performance of the MuFO system under broad ranges of temperature and water saturation, as may be found in cold temperature soils.

2.7 Soil CO2 Flux Measurement

Following the procedure used by Rezanezhad *et al.* (2014), the CO_2 efflux measurements were taken from headspace of the soil columns every 1-2 days. This was done using an automated multiplexer CO_2 flux measurement system (LI-8100, LI-COR Biosciences, Lincoln, NE, USA), which was connected to the column headspace by two lateral ports (see Figure 9).

The column ports enabling gas exchange between the headspace and atmospheric air were closed during the sampling period so only the headspace air was measured by the infrared gas analyzer (IRGA) of the LI-8100. This air was then circulated back to the headspace. The rate of increase in CO_2 concentration in the closed off headspace ($dCco_2/dt$, µmol mol^{-1} s^{-1}) is used to calculate the flux of CO_2, F_{CO2} (µmol m^{-2} s^{-1}), from the soil by the following relationship:

$$F_{CO_2} = \frac{PV}{RT_{CO2}S}\frac{dC_{CO_2}}{dt} \qquad (13)$$

where, R is the gas constant (8.314 Pa m^3 $°K^{-1}$ mol^{-1}), S (m^2) is the soil surface area exposed at the top of the column, T_{CO2} is the absolute temperature (°K), P is the atmospheric pressure (Pa), and V (m^3) is the headspace volume in addition to the volume of the tubing through which the gas sample was circulating (Rezanezhad *et al*., 2014). Note that the temperature for the CO_2 flux is in Kelvin as opposed degrees centigrade (used for all other temperature calculations). Each sampling session was conducted over 30 minutes, which was used as the time for estimating the $dCco_2/dt$ rate.

CHAPTER 3: RESULTS

3.1 MuFO Parameters and Performance

The MuFO performed consistently in both experiments from the beginning to the end of each trial. The performance parameters for the MuFO sensor are shown in Table 2 and were determined using data from the calibrations and results from both experiments. Parameters presented include: precision, range, repeatability (general observation), drift, limit of detection (LOD) and quantitation (LOQ), sensitivity, and spatial resolution.

Following the work of Badocco and Pastore (2008), the **precision** of the MuFO system is represented by the first derivative of $\Delta I_{\%}/\%O_2$ shown in Figure 12, where the results of equation 14 at various *K'sv* values are plotted as a function of oxygen.

$$\Delta I_{\%} = \frac{100}{1+\frac{10^{pK'sv}}{\%O_2}} \qquad (14)$$

In equation 14, *pK'sv* = - log (*K'sv*). The *K'sv* value selected is based on an average of 16 sensor calibration (standard deviation of 0.0018), which was done in addition to the calibrations for the WT and FTC experiment. The *pK'sv* value for a *K'sv* of 0.006 is 2.2. The resulting precision is shown to decrease by 0.0036 for each percent increase in O_2, consistently across the full **range** of saturation from 0 % to 100 %, as seen in Figure 12. This is also based on the average of 16 sensor calibrations and, while each sensor is unique, this result is a good approximation of the level of precision that can be expected and indicates usability over the full range of oxygen saturation.

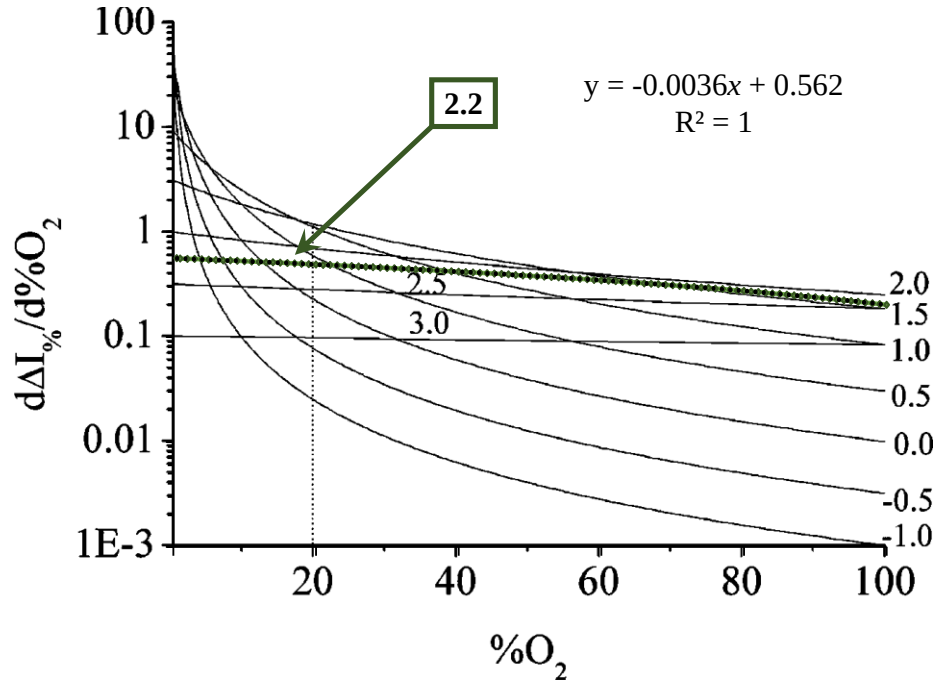

Figure 12: First derivative of change in intensity (relative to I_o) with change in $\%O_2$ for *pK'sv* value of 2.2 overlain on Figure 6 from Badocco and Pastore (2008). Equation of *pK'sv* = 2.2 line shown.

From the experimental data results, the sensors each showed good **repeatability** in values measured during each cycle of freeze-thaw as well as unsaturated and saturated conditions. Under saturated conditions, all sensors recorded values near 0 % and not more than 3 % in both the WT and FTC experiments. However, the values of O_2 saturation in the unsaturated zone of the FTC column (regardless of temperature) and during the drainage period in the WT experiments were more varied than under saturated conditions. For example, while under unsaturated conditions, the readings ranged between 45 % and 80 % O_2 saturation.

The **drift** was measured based on the control soil column in the WT experiment and from the greatest depth in the saturated zone of the freeze-thaw experiment - both locations where the oxygen was low and would not be expected to fluctuate much. This way, any change in signal emission over time could be attributed directly to sensor drift (*e.g.* due to photobleaching from overexposure to the excitation light source) rather than external influences on the oxygen concentrations.

In the WT experiment, drift in anoxic readings (taken from the sensors at -27.5 cm below the soil surface, between 7 and 14 days, when the region was saturated with water) showed the

percent difference between the maximum and minimum readings during this period to be less than 0.02 %. In the unsaturated zone the readings taken from the sensor at -6.5 cm between day 0 and day 12, showed the difference in intensity values to be approximately 1 %. The oxygen levels in the saturated zone measured at depths of -28 cm and -40 cm in the freeze-thaw soil column stabilized after 31.5 hours (~1.3 days). For the remaining 37.7 days these values did not display any measurable drift and duplicates at each saturated depths differed in units of intensity by a maximum of 3.4 (0.7 $\%O_2$) and 3.8 (0.8 $\%O_2$), respectively. In the water table fluctuation column, drift could be monitored from the control column data.

Periodically, a uniform step-wise change in intensity signal was detected in the constant (saturated and control column) comparisons. This generally occurred in sudden uniform shifts as opposed to a gradual change. For instance, at -21.5 cm in the control column, the intensity signal decreased from an average of 120 a.u. to 118 a.u. at 19.2 days. These signal jumps could be easily corrected by applying a subtraction, based on values from the control sensors, to bring the raw intensity values back to stable pre-drift levels. This was only applied when the signal change was detected across the sensor network. Since the jump was seen in all sensors simultaneously, this drift was likely due to an electronic issue in the LED or camera. No drift caused by sensor degradation was detected during these two experiments.

The **LOD** and **LOQ** were determined using the method found in Apostol *et al.* (2009), following the International Conference on Harmonization (ICH) Q2R1 guideline. In the ICH Q2R1 guideline (2005) the LOD is defined as ‘‘*the lowest amount of analyte in a sample which can be detected but not necessarily quantitated as an exact value.*” The LOQ is defined as ‘‘*the lowest amount of analyte in a sample which can be quantitatively determined with suitable precision and accuracy,*” (ICH guideline Q2R1, 2005). The data used for the required blank values were from the measurements recorded at the saturated depth of -40 cm in the freeze-thaw column. This was considered reasonable since microbial respiration is highly effective in depleting oxygen (Norris and Ribbons, 1969). The variation between duplicate intensity values was ≤0.3 % for all sensors, regardless of temperature or saturation.

Sensitivity of the sensors to oxygen saturation is indicated by the *K'sv* values. The *K'sv* values for the WT experiment, shown in Table 1 of Chapter 2, were unique to each sensor. The value used for all of the sensors in the FTC experiment was 0.006, indicating (for linear relations) that the intensity, I, decreases by 0.006 a.u. for every percent increase in oxygen.

The intensity showed sensitivity to temperature as well. As seen in Figure 5 (Chapter 2), the ratio between the Io value and the I values at each oxygen level increased overall with increasing temperature, confirming light intensity sensitivity to the temperature variation. Put another way, the range of intensity (Io to I_{100}, which denotes at 100 % air saturation with oxygen), decreased with decreasing temperature by 0.6 intensity units. This was however, only based on one set of temperature calibrations and would need to be verified. That said, this result is similar to that found by Lo *et al.*, (2008) and Badocco *et al.* (2012), who conducted temperature trials over ranges of 25 °C to 70 °C and 40 °C to 90 °C, respectively.

Parameter	Value	Method	Reference
Precision[2]	$\frac{d(\Delta I_{\%})}{d\%O_2} = -0.0036(\%O_2) + 0.562$	First derivative of $\Delta I_{\%}$ by $\%O_2$	Badocco and Pastore, 2008
Range	0 – 100% O_2	Linear relation of precision method	Badocco and Pastore, 2008
Limit of Detection	0.2 $\%O_2$ saturation, for 4 to 10°C	3.3 x range of noise in blank at 0 $\%O_2$	Apostol *et al.*, 2009
Limit of Quantitation	0.6 $\%O_2$ saturation, for 4 to 10°C	10 x range of noise in blank at 0 $\%O_2$	Apostol *et al.*, 2009
Sensitivity to change in O_2	See Table 1 for water table sensors; *K'sv* = 0.006 for freeze-thaw	*K'sv* value (intensity change per unit change in oxygen)	Wang and Wolfbeis, 2014
Sensitivity to temperature	Intensity range (I_0 to I_{100})increases by 0.6 units per °C increase (R^2=0.974)	Temperature calibration	n/a
Spatial resolution	0.785 mm² for one sensor of 1 mm diameter	Surface area of entire sensor tip	n/a
Drift	No drift detected	Visual inspection of *I* changes over time	n/a
Duplicate values	% difference ≤ 0.3 % between duplicate intensity values*	Variation between max and min *I*'s	n/a

Table 2: Performance parameters of MuFO method. *The value of 0.3 % is under stable oxygen levels; this value can increase to 10 % during transitions in oxygen levels, indicating limitation in temporal resolution to capture rapidly occurring changes.

[2] This is for the theoretical *pK'sv* value of 2.2, across full range of 0 % to 100 % oxygen saturation.

Regarding the **spatial resolution**, the finest spatial resolution that can be obtained is ultimately equal to the pixel size, which is 0.00527 mm^2. However, this can only be used if the camera does not move at all over the measurement time, otherwise different portions of the sample will be measured in the images where there was camera movement. Thus, a more appropriate constraint for determining a representative spatial resolution is not the pixel size, but rather the surface area of the entire sensor tip (1 mm diameter), which is the next smallest uniform unit for comparison. While this can be the upper limit in spatial resolution, numerous sensors can be aligned parallel to each other to increase the monitored area.

3.2 Water Table Fluctuation Results

The data from the WT experiment presented here include the O_2 saturation monitored at various depths (Figure 13 and Figure 14) and the corresponding CO_2 efflux data collected from the soil column headspace under the water table regime (Figure 15).

3.2.1 Oxygen Data

Figure 13 and Figure 14 show the O_2 saturation data collected by the MuFO system during the WT experiment. Figure 13 shows data at three depths, -6.5 cm, -12.5 cm, and -27.5 cm, for two of the four complete water table saturation-drainage cycles, while Figure 14 shows the data at all monitored depths during the increase in water table from day 10 until day 12.7.

In Figure 13, the O_2 levels at each depth changed with the water table changes. However, the changes in the O_2 saturation remained steady at the new high or low O_2 levels while the water level in the equilibrium column changed constantly and never stabilized at one level.

The O_2 saturation at each depth in the soil column followed repeatable patterns with each water table fluctuation, but the patterns were unique at each depth. Starting from day 10 to 12.5, as the water table was rising, the O_2 saturation at -27.5 cm remained at 0 %, indicating that this level was already saturated at this time. The first response of the O_2 concentration to the water table displayed in Figure 13 was at -12.5 cm: O_2 decreased from 71 % at day 11.9 to 0 % by day 12.8 at a rate of -3.3 % hr^{-1}, followed by a decrease at -6.5 cm from 75 %

at day 12.2 to 0 % by day 12.8 at a rate of -5.2 % hr^{-1}. From day 12.5 to 15.0, as the water table dropped, the O_2 saturation remained close to 0 % at each depth, then increased sequentially. First, at day 13.9 the O_2 saturation at -6.5 cm increased to 74 % where it stabilized. At day 14.6, the O_2 saturation at -12.5 cm reached 66 % and stabilized at about 70 % by day 15. Finally, the O_2 saturation at -27.5 cm increased very rapidly to reach approximately 48 % by day 14.6.

During the next water table increase shown in Figure 13 from day 15 to day 17.5, the O_2 saturation at -27.5 cm was the first to respond, decreasing from 48 % on day 16.5 to 0 % by day 17 at a rate of -1.1 % hr^{-1}. The O_2 saturation at -12.5 cm was the next to decrease from 69 % on day 16.9 to reach 0 % by day 17.7 (rate of -3.6 % hr^{-1}). This was closely followed by the decrease in O_2 saturation at -6.5 cm from 73 % on day 17.1 to 0 % by day 17.9 (-3.8 % hr^{-1}). During the final phase of this cycle from day 17.5 to day 20, the water table increased. The first observed response was at -6.5 cm, where the O_2 saturation increased from 0% at day 18.0 to reach 75 % by day 18.2 (rate of +15.6 % hr^{-1}), where it remained for the rest of the cycle. The O_2 saturation at -12.5 cm and -27.5 cm increased at day 19.2 to stabilize at 67 % by day 19.5 (+14 % hr^{-1}) and at day 19.1 to reach 47 % by day 19.3 (+9.8 % hr^{-1}), respectively.

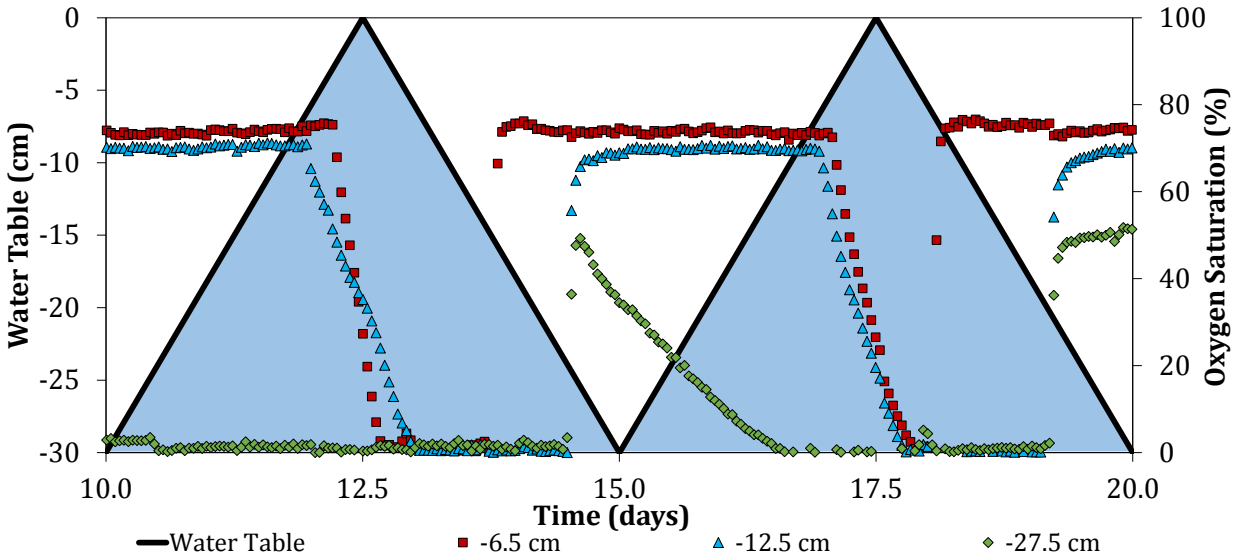

Figure 13: Oxygen dynamics at different depths in the soil column during the third and fourth complete water table fluctuation.

Figure 14 shows the depth profiles of O_2 saturation in the soil column under one water table fluctuation phase. Profiles of O_2 saturation at different depths in the soil column are shown for five water table conditions corresponding to O_2 saturation values at various points in time, from Figure 13. The O_2 levels at a water table of -30 cm (Figure 14a) show a higher O_2 saturation with increasing proximity to the soil surface. The O_2 levels at -27.5 cm were never greater than 1 % at all water levels indicated. The O_2 saturation decreased at progressively shallower soil depths as the water table moved up the column. By the time the water table was raised to -2 cm (Figure 14e) the O_2 values were below 5 % at all depths except at the depth of -18.5 cm, which, surprisingly, only decreased by about 40 % O_2 saturation from 60 % at a -30 cm water table to 20 % at a -2 cm water table.

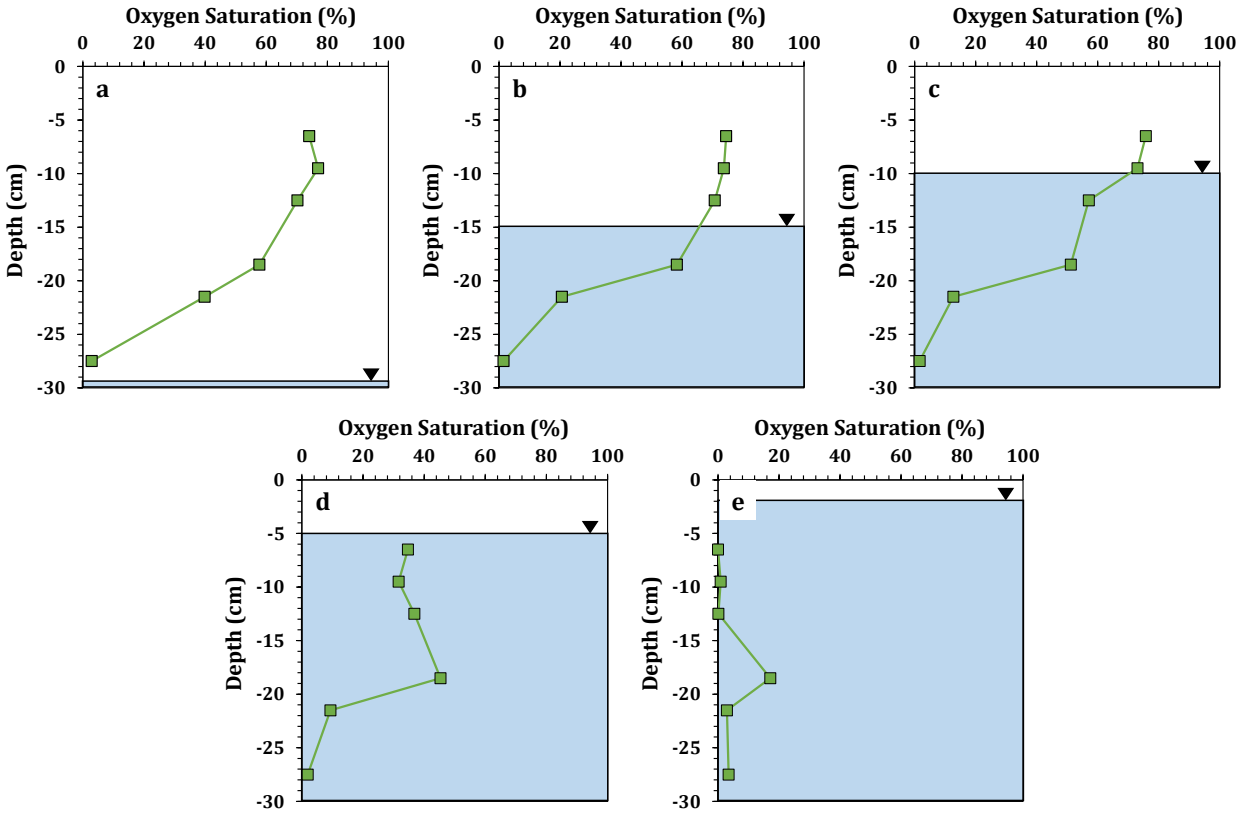

Figure 14: Oxygen saturation (% in air) at -6.5 cm, -9.5 cm, -12.5 cm, -18.5 cm, -21.5 cm, and -27.5 cm from the soil surface when the water table is at: a) -30 cm (day 10), b) -15 cm (day 11.6), c) -10 cm (day 12), d) -5 cm (day 12.5), and e) -2 cm (day 13.7).

3.2.2 Water Table Fluctuation Regime

The dynamic water table levels were imposed on the soil column with the aid of an equilibrium water column and was meant to follow the trend shown in Figure 13, where the water level was alternatively increased over a period of 2.5 days to saturate the soil and subsequently decreased over 2.5 days to drain the soil across the full length of 30 cm of the column. The rate of increase and decrease was set to be constant at about 12 cm day^{-1}. The actual rate was difficult to control due to technical difficulties with the peristaltic pump and equilibrium column connections, so while it was close to the intended rate on average, it did vary between the saturation (slower) and drainage periods (faster). This was not measured, but was seen (by visual inspection) in the soil and water columns and the response (or lack thereof) in a few of the oxygen sensors at the top and bottom of the soil column.

3.2.3 Carbon Dioxide Data

The CO_2 efflux data over the 20-days WT experiment are shown in Figure 15. These data were collected in the headspace of the column and are an expression of the CO_2 efflux from the soil column. It can be seen that, overall, the efflux was larger under unsaturated conditions than saturated conditions. With subsequent cycles, the maximum magnitude of the CO_2 efflux decreased from a maximum of approximately 0.51 μmol m^{-2} s^{-1} at day 0 to a maximum of 0.22 μmol m^{-2} s^{-1} at day 19. Meanwhile, the effluxes measured during the saturated periods were always below 0.06 μmol m^{-2} s^{-1}, but were never less than 0.01 μmol m^{-2} s^{-1}. These trends resulted in a decrease in the difference between the emitted CO_2 efflux captured during the saturated and unsaturated conditions. The CO_2 effluxes increased and decreased in a similar manner with the exception of a pulse (indicated by a large increase in CO_2 emission over a short time) in the first drainage event, just before day 5 (Figure 15).

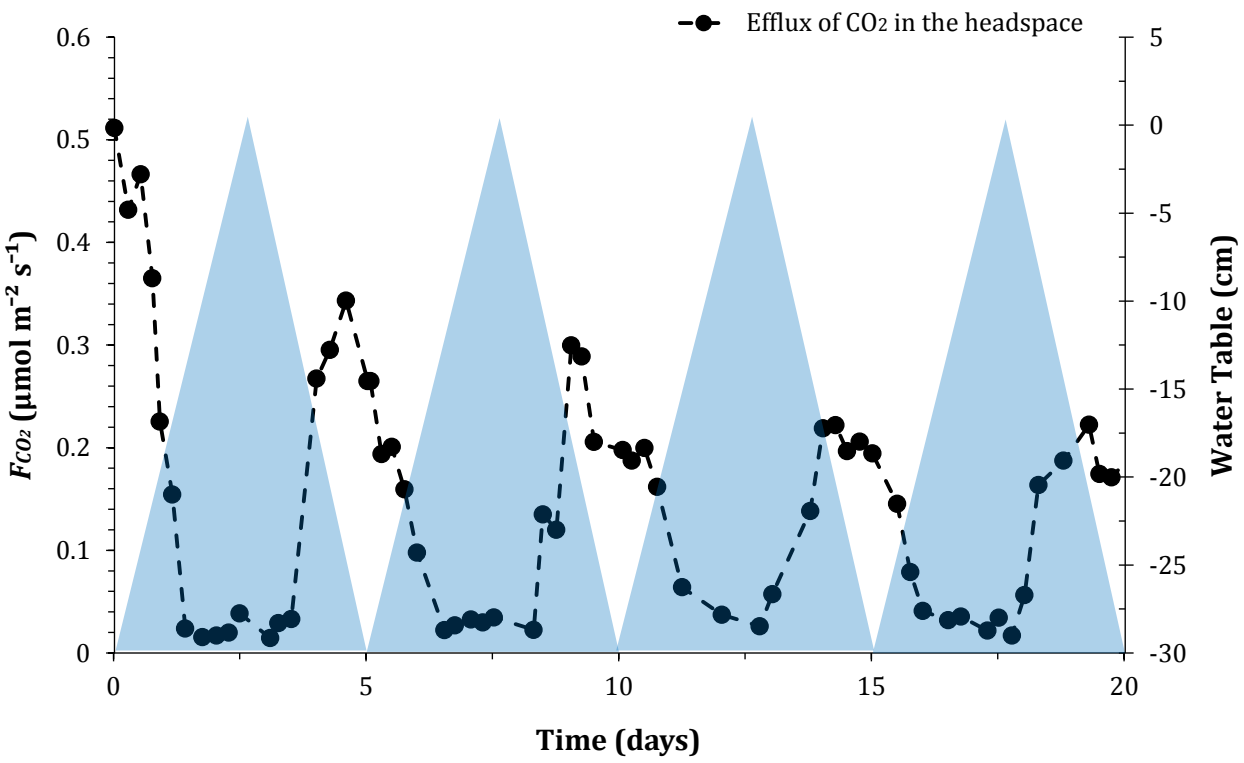

Figure 15: Efflux of CO_2 in the water table fluctuating soil column plotted as a function of time. The large variations of the CO_2 emissions correlate with the imposed water table fluctuations where the CO_2 emission peaks occurred during low water table. The plot also shows the water level in the equilibrium column.

3.3 Freeze-Thaw Cycle Results

The freeze-thaw experimental results summarized here include the O_2 data monitored at various depths throughout the soil column, the temperature regime monitored from the air, unsaturated soil and saturated soil, and the CO_2 efflux measured in the column headspace.

3.3.1 Oxygen Data

Figure 16 and Figure 17a show O_2 saturation data at various depths within the soil column during one complete freezing and thawing cycle, which occurred between days 21 and 27. Figure 16 shows a typical depth profile in the freeze-thaw cycle experiment. The trends with depth of the frozen and thawed O_2 saturation levels are similar. Average values of O_2 saturation are shown for depths of -1 cm, -7 cm, -10 cm, -16 cm, -28 cm, and -40 cm from the soil surface. For each depth, the averages are calculated based on the O_2 saturation values

from day 24.4 to day 27.0 for the "Thawed" profile and from day 27.5 to day 30.0 for the "Frozen" profile. These data from the MuFO sensor show the O_2 to be depleted at -16 cm, -28 cm, and -40 cm in the lower portion of the column, which was kept fully saturated (water table at -8 cm) and at a constant temperature for the duration of the experiment. These values were less than 1 % (±0.1 %) O_2 saturation and there was not clear difference between the frozen and thawed periods. There was a difference between the frozen and thawed values, however, at the depths points monitored at -10 cm and above. The discrepancy increased with increasing proximity to the soil surface. At -10 cm, the O_2 saturation was approximately 30 % on average (±0.3 %) during the frozen period and about 38 % on average (±1.5 %) during the thaw period. Just above the water table, at -7 cm, the O_2 saturation was approximately 63 % on average (±1.5 %) during the frozen period and about 80 % on average (±2.1 %) during the thaw period. Finally, at -1 cm, the O_2 saturation was 66 % on average (±0.6 %) during the frozen period and 84 % on average (±0.2 %) during the thaw period. Note that the uncertainties shown in brackets correspond to the standard deviation for each averaged set.

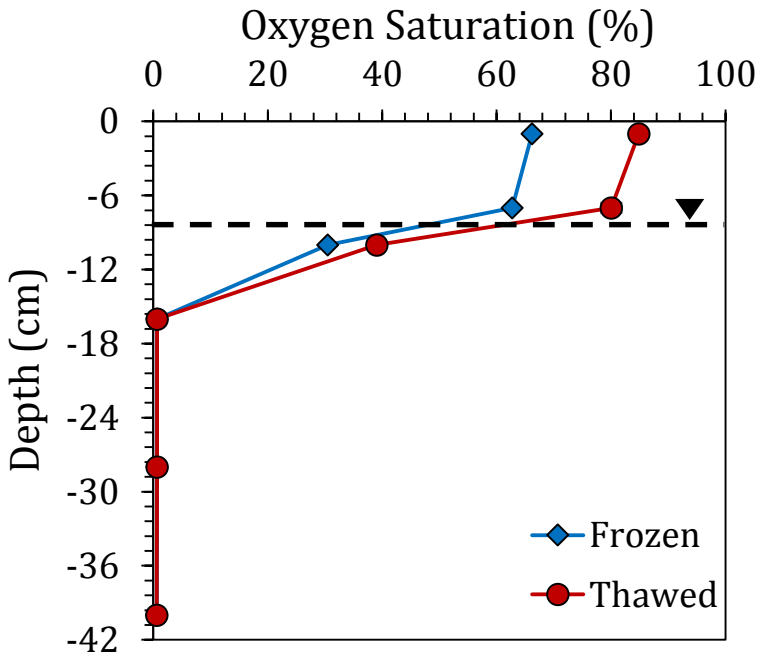

Figure 16: Depth profile of oxygen saturation in the soil column under a freeze-thaw cycle from day 21 to 27. Values shown represent the average values at each depth during the thawed and, separately, the frozen periods. Standard deviations on values shown fall within the symbol sizes.

Figure 17a shows the O_2 saturation for each of the monitored depths in the FTC soil column over a full cycle of freezing and thawing and a subsequent freezing period. This way the dynamic influences of the temperature (Figure 17b) can be compared. Figure 17a shows a consistent trend of the O_2 saturation over time. For ease of reference, the frozen periods are indicated by the blue background while the pink background is indicative of the thaw period.

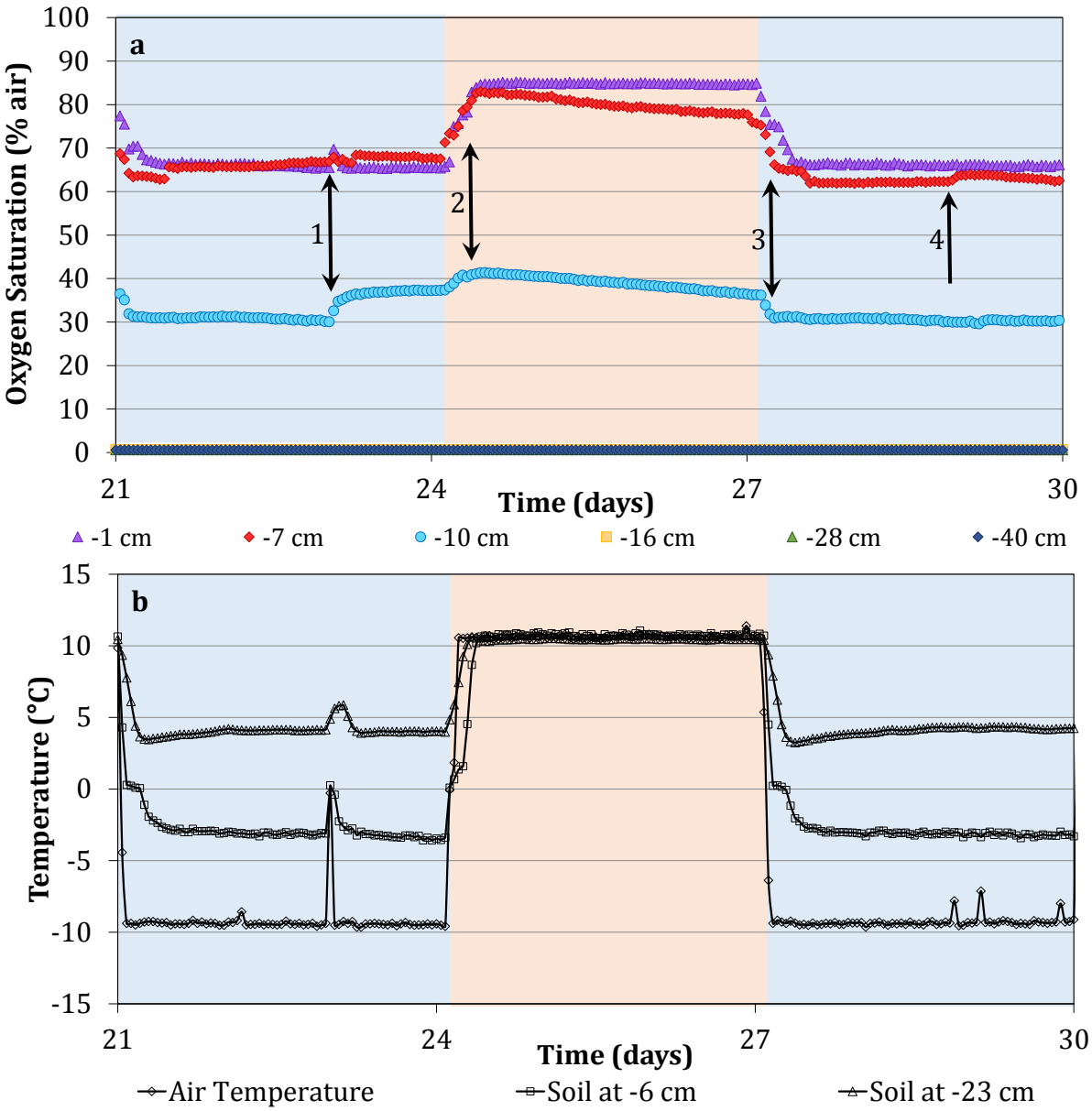

Figure 17: Oxygen dynamics (a) at different depths in the soil column during the fourth complete freeze-thaw cycle. The water level in the soil column was at -8 cm below the soil surface but fluctuated perceptibly during water sampling events (arrows 1 and 4). The sampling event indicated by arrow 1 also led to a temporary increase in soil temperature (b) at depth due to the sampling procedure. Peaks in oxygen data (arrows 2 and 3) follow temperature changes in the system.

In the saturated zone (at -40 cm, -28 cm, and -16 cm) O_2 saturation remained close to zero, as displayed in Figure 17a. No changes in the O_2 saturation in this lower portion of the soil column were observed for the duration of the experiment. In the unsaturated zone (at -10 cm, -7 cm, and -1 cm) the O_2 changed as the temperatures fluctuated during the freezing and thawing periods in a pattern that was repeated during each cycle, where O_2 saturation was higher during thaw conditions. Here O_2 saturation was up to 20 % greater during the thaw period compared to the frozen period. While this general trend was common in the top three monitored points (-1 cm, -7 cm, -10 cm), the individual patterns at each depth varied.

Just below the soil surface (-1 cm), the O_2 saturation was fairly stable at about 65 % (±0.6 %). This difference does not include the brief spike (maximum value to 70 % saturation) in O_2 that can be seen at day 23, indicated by the arrow at point 1. No such spike was seen in the rest of the O_2 for this cycle. As indicated by arrow 2, the O_2 saturation increased over 8.2 hours at a rate of (+1.25 % hr^{-1}) to 85 % where it remained stable until the next freeze period. The decrease in O_2 saturation during this subsequent freeze cycle (arrow 3) occurred over 6.2 hours at a rate of (-1.6 % hr^{-1}). The O_2 saturation remained steady at 67 % for the rest of the period.

Closer to the water table, the sensors found at -7 cm and -10 cm from the soil surface both followed a similar trend. At -7 cm, just above the water table, the O_2 saturation was between 63 % and 68 % between days 21 to 24, with the maximum O_2 level occurring at day 23, similar to the spike seen in the -1 cm data. At the start of the thaw period, the O_2 saturation increased over 6.2 hours at a rate of +1.6 % hr^{-1} to a maximum value of 83 %. Unlike the point at -1 cm, following this increase, the O_2 levels at -7 cm steadily decreased over 63 hours (at -0.1 % hr^{-1}) to a minimum value of 75 %. Then, with the onset of the next freeze cycle, the O_2 saturated dropped in a similar pattern as the temperature decreased at -7 cm (Figure 7b); first to 65 % then, following a brief stable period (lasting 7.2 hours), dropped again, to 62 %. For the remainder of the freeze period, the O_2 saturation was at 62 % and then increased slightly to 63 % at day 29 (indicated by arrow 4 on Figure 17a) before gradually decreasing back to 62 % by day 30.

The O_2 saturation data at -10 cm from the soil surface followed a similar trend to that at -7 cm. During the freeze period beginning at about day 21, the O_2 saturation hovered around 31 %. It then increased at day 23 (point 1 in Figure 17a) to about 35 % O_2 saturation, where it remained fairly steady until the next increase to 41 % with the onset of the thaw period (arrow point 2). Like the O_2 saturation at -7 cm, the % saturation decreased steadily over the 64 hour thaw period at a rate of -0.1 % hr^{-1}. With the onset of the next freeze cycle (point 3), the O_2 saturation decreased over 3 hours to reach 31 % O_2 saturation by day 27.2. The O_2 saturation remained near this level for the rest of this frozen period.

3.3.2 Temperature Regime

The column set-up worked well to direct freezing in the unsaturated zone while keeping the saturated zone above zero degrees centigrade (Appendix A5 and A6). The temperature data for one complete freeze-thaw cycle in shown in Figure 17b. During the freezing and thawing cycles larger and more rapid variations in O_2 concentrations at the depths close to the soil surface (-1, -7 and -10 cm). The air temperature in the chamber changed fastest, increasing/decreasing by about 20 °C (between about -10 °C and 10 °C) over a period of approximately 1.0 to 1.5 hours, depending on the cycle. The unsaturated soil temperature measured at -6 cm from the soil surface changed by about 13°C (from -3 °C to 10 °C) over a period of about 9.5 hours overall. However, this change was not evenly distributed with time, particularly as the temperature deceased. During freezing, about 75 % of the change in temperature occurred over 2.5 hours until the temperature approached zero degrees and then the remaining 25 % drop in temperature proceeded over about 7 hours. A similar pattern is seen as the soil thaws from a temperature of about -3 °C, in that the thaw occurs rapidly (over 1 hour) until 0 °C is reached and then slows (increasing by 1.5 °C over 3.5 hours or by a rate of 0.4 °C hr^{-1}), but quickly increases again by 9 °C over 5 hours (rate of about 1.8 °C hr^{-1}). This general trend is repeated for all FTC at this depth. At the greatest monitored depth (-23 cm from the surface), the temperature change is experienced gradually. The temperature change is the same during the freezing and thawing processes, decreasing and increasing, respectively, by 6 °C (between about 4 °C and 10 °C) over a period of 7 hours. The rate of change of 0.9 1.8 °C hr^{-1} is consistent over this time.

Once the temperature was established in each period of freezing or thawing there was little change, unless outside influences affected the chamber temperature. During the thaw period the temperature at each depth remained consistent with the average difference between the maximum and minimum values being 0.5 °C (±0.2 °C). However, under the frozen condition, the temperature did increase when there was an external disturbance, which drastically changed the temperature (*e.g*. opening the chamber door for sampling and exposing the column to room temperature). This effect is not seen during thaw periods.

3.3.3 Carbon Dioxide Data

The CO_2 efflux data for the duration of the freeze-thaw experiment (39 days) are shown in Figure 18. This data represents the efflux of CO_2 from the soil column as measured in the headspace of the column. Generally, it can be seen that the efflux is greater during the thawed condition as opposed to the frozen period. With subsequent cycles, the maximum magnitude of the CO_2 efflux decreased from a maximum of 0.26 μmol m^{-2} s^{-1} at 6.5 days to a maximum of 0.07 μmol m^{-2} s^{-1} at 36.5 days. In contrast, the efflux measured during each of the frozen periods rarely exceeded 0.05 μmol m^{-2} s^{-1}, though they never fell below 0.01 μmol m^{-2} s^{-1}. Thus, over time the difference between the CO_2 efflux during the thawed and frozen periods decreased. Of particular interest is the large pulse in CO_2 efflux that was captured in the first thawing period following the first frozen period. While subsequent thaw events showed increases in CO_2 efflux relative to their preceding freeze periods, the same spike in CO_2 was not captured as clearly in the remaining cycles as it was in the thaw following the first freeze period.

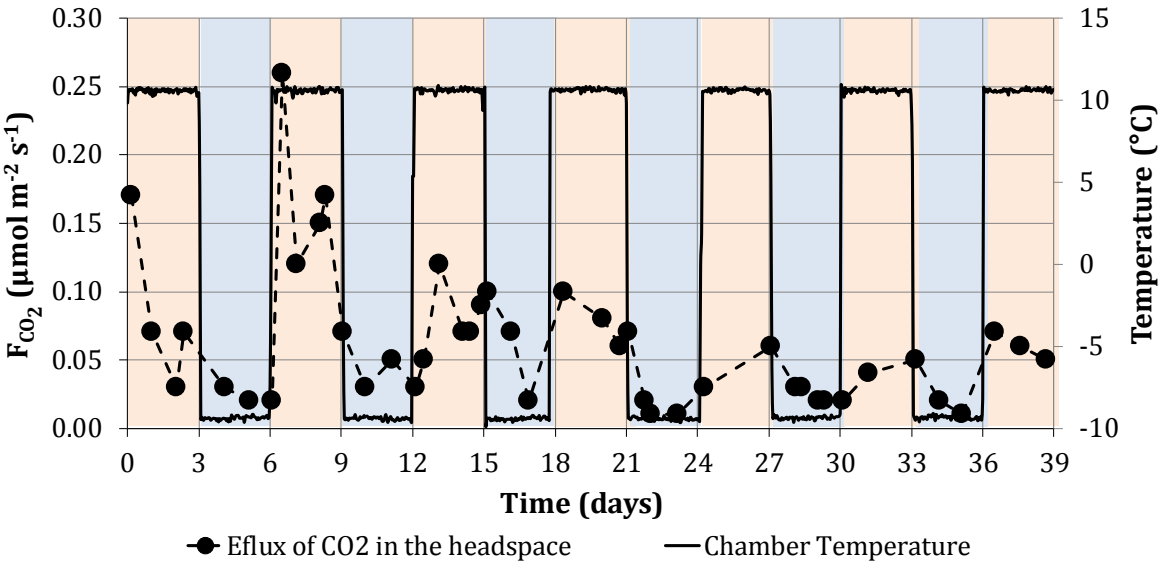

Figure 18: Efflux of CO_2 in the freeze-thaw soil column plotted as a function of time. The large variations of the CO_2 emissions correlated with the imposed temperature fluctuations where the CO_2 emission peaks occurred during thawing. The plot also shows the chamber temperature.

CHAPTER 4: DISCUSSION

4.1 MuFO Method

A primary focus of this research was the development of an affordable oxygen optode system for use in laboratory experiments, specifically soil column experiments with variable water saturation and soil temperature. While many methods for O_2 measurement exist, the optode system was selected for the benefits it has over traditional approaches (see Chapter 1). The MuFO was implemented in the WT and FTC experiments to evaluate its use as a tool to monitor O_2. The system was judged on affordability, technical specifications, and operability.

4.1.1 Affordability

The MuFO system is affordable and ideal for researchers looking for a tool to monitor O_2 in gaseous and/or dissolved form. The cost of the system amounted to less than $2,500.00 (Canadian dollars). This price excludes the costs of the computer (required for imaging and digital image processing) and the costs of building the support block, external box cover, and connecting the LED to the trigger box wire. These tasks were completed by machine shop technicians and electricians at the University of Waterloo. However, even with the inclusion of these labour costs, the total price would be a few thousand dollar less than the closest competitor, as seen in Table 3. Moreover, the one-time cost of the interrogation system (*i.e.* LED, digital camera, and trigger box) is less than the oxygen meter (corresponding interrogation system) of the closest listed competitor. In addition, due to the simple design, the sensing tips can be cut off after use (or if damaged) and the optode coating can be applied to a fresh tip of the same fibre optic cable. This process can be repeated until the fibre optic cable length is inadequate (*e.g.* too short to reach the desired soil depth) and thus, minimizes the waste resulting from each new sensor.

4.1.2 Technical Specifications

As previously stated in Chapter 3, the MuFO performance was consistent for the duration of both experiments. Drift in intensity signal over time has been seen in other optode system

tests (albeit with higher measurement frequency) such as that developed by Badocco *et al.* (2013a, 2013b), who also provided an algorithm for drift correction. In the case of the MuFO deployed in the WT and FTC experiments here, no drift caused by sensor degradation was detected. This may be attributed to the frequency with which the LED was pulsed, the longer time between measurements (*e.g.* one each hour), and the duration of the experiment (20 and 39 days). However, uniform step-wise shifts in intensity were periodically seen in the emission data and were corrected by bringing the raw intensity values back to pre-drift levels based on the values from the control sensors. Since the shift observed was uniform in all sensors simultaneously, this drift was probably due to a change in the LED excitation light or (less likely) camera malfunction. As such, this MuFO set-up might be recommended for longer term experiments, provided the measurement frequency and luminophore exposure to light is appropriately limited. Should any drift in intensity signal be noticed, a correction may be necessary.

The MuFO sensor can measure O_2 in the full range from 0 % to 100 % O_2 saturation. This was ideal for the soil column experiments presented. A consequence of the wide range in that the sensor has a lower precision as a result (shown previously in Table 2 and Figure 12). Precision can, however, be modified by using multiple sensing species in the sensing matrix (Badocco and Pastore, 2008). This helps to increase sensitivity to O_2 changes for experiments requiring trace measurements in addition to high O_2 level readings. Another option is to develop trace sensors to separately measure lower O_2 levels, as seen in the offering by Pyroscience (Table 3), but measurement range might be sacrificed as a result of lower precision at high O_2 levels.

Sensitivity of the MuFO system to O_2 is represented by the *K'sv* values shown in Table 2, which is lower than values from a similar PtTFPP-based sensor reported in the range of 0.150 and 0.167 by Badocco *et al.* (2009, 2012). Badocco *et al.* (2012) show how increasing temperature leads to an increase in *K'sv* for a PtTFPP-based sensor, hence increasing the measured range of intensity values for 0 % to 100 % O_2 at temperatures between 40 °C and 90 °C. This relationship is similar to that observed in this MuFO method as measured between 25 °C and -10 °C. The calculated precision varies slightly with O_2 levels as shown in

Table 2 (Chapter 3). Unfortunately, the commercial sensors shown in Table 3 did not report values of precision for comparison. The LOD of the MuFO system is 0.2 $\%O_2$, which is much higher than the commercial sensors (Table 3), showing that this sensor is best suited to use in systems with broader oxygen dynamic investigations not requiring low level O_2 detection.

Company	MuFO	Pyroscience	PreSens	Unisense
Cost (Can$)	2,327.07	33,793.80[3]	40,060.60[4]	53,821.90[5]
Measurement Range	0 – 100 $\%O_2$	0 – 50 $\%O_2$ (normal) 0 –10 $\%O_2$ (trace)	0 – 100 $\%O_2$	0-100 $\%O_2$ 0-50 $\%O_2$ (optimal)
Limit of Detection	0.2 $\%O_2$	Not specified	0.03 $\%O_2$ (gaseous and dissolved)	0.02 $\%O_2$
Accuracy (at 20 $\%O_2$)	*0.11 $\%O_2$ (%RSD<5 %)	±0.2 $\%O_2$ (at 20 $\%O_2$)	±0.4 $\%O_2$ (at 20.9 $\%O_2$)	±2 $\%O_2$ (at 20 $\%O_2$)
Accuracy (at ≤ 1 $\%O_2$)		±0.05 $\%O_2$ (at 1 $\%O_2$)	±0.05 $\%O_2$ (at 0.2 $\%O_2$)	±0.02 $\%O_2$ (at 1 $\%O_2$)
Operational Temperatures (specified)	-10 °C to 25 °C (tested range)	0 °C to 50 °C	0 °C to 50 °C	0 °C to 50 °C
Reference	*Badocco *et al.*, 2012	Quoted price (Pyroscience, 2016)	Quoted price (PreSens, 2016)	Quoted price (Unisense, 2016)

Table 3: Comparison of oxygen optode systems available commercially with the MuFO system built in-house. To standardize the comparison, the presented prices are for a total of 16 oxygen sensors. All final costs exclude shipping and tax. *Accuracy listed is not for this MuFO sensor but for a similar sensor made by Badocco *et al.* (2012).

[3] Converted from quoted price of 5,720.00 € (shipping excluded) using the Bank of Canada rate of 1.4770 (closing rate of euro to Canadian dollar on October 5th, 2016). This price includes one meter (FireStingO2 (4 channels), fibre optical oxygen meter, incl. USB-cable, logger software (Windows) and transport case) priced at 4,480.00 €, one temperature sensor (Temperature sensor for FireStingO2, Teflon-coated and submersible, not shielded, ca. Ø2.1mm, 2m cable) priced at 160.00 €, and 4 oxygen probes (270.00 € each) priced at 1,080.00 €. The total sum converted into Canadian Dollars is $8,448.44. For 16 probes, this values is multiplied by 4.

[4] Cost for PreSens system comprises one oxygen meter (*Prototype* OXY-4 SMA 4-channel fibre optic oxygen transmitter) priced at 4,990.00 € and four dipping probes (DP-PSt3-L2.5-St10-YOP Oxygen Dipping Probe) priced at 490.00 € each. Note that this oxygen meter is considered a custom-built to accommodate 4 sensors (the alternative is the Fibox 4 oxygen meter, priced at 3,990.00 €). The total cost in Canadian dollars amounts to $10,265.15. For 16 probes, this values is multiplied by 4.

[5] Cost for Unisense system amounted to 4,450.00 €, which comprised of one MicroOptode Meter (3,800.00 €), two Oxygen MicroOptode 430 µm Retractable Needles (320.00 € each), and one Temperature Sensor for the MicroOptode Meter (115.00 €). The total cost in Canadian dollars is $6,727.74. For 16 sensors, this value is multiplied by 8.

In the calibration tests, the intensity range diminished by 0.6 units of intensity per decrease in degree centigrade, however the test should be repeated several more times to get a better constraint on the relationship between the temperature (particularly sub-zero values) and the MuFO sensing capabilities. For this study, temperature effects were directly corrected using the *C(T)* correction factor described in Chapter 2. These corrections were dependent on additional temperature probe measurements. Similarly, many commercial sensors require additional temperature probes (if they are not already incorporated into the sensor) to compensate for temperature variations. This approach is based on the assumption that the temperature probe is close enough to the O_2 sensor location to be representative of the temperature at the oxygen measurement point. Both O_2 and temperature sensitivities from the MuFO sensor are in line with the general range of values found by Wang and Wolfbeis (2014) for optical sensors, but are not particularly competitive as an optode technique based on this alone.

4.1.3 Operability

While proper calibration can be time consuming (about one hour per sensor if done separately for each sensor), the overall process of sensor manufacture and operation is fairly straightforward, although more effort-intensive than using commercially available (*i.e.* pre-made) optodes. Yet, building an MuFO type system allows the user greater flexibility and control in design and the application of the system as well as a better understanding of the operability making it easier to troubleshoot any errors.

Errors commonly encountered with this system include optode errors and technological errors. Optode errors can be caused by many factors, including: physical degradation of the matrix, photobleaching of the luminophore, heterogeneities in the sensor film, and interferences discussed in Chapter 2. Technological errors are due to computer, LED, trigger box, or camera malfunctions and usually indicated by gaps in the data set or ubiquitous shifts in intensity values. This is why, despite the additional work, it is ideal, to have a reference sensor outside of the experimental sample to help catch data shifts and, for long term experiments, drift.

In comparison to traditional O_2 measuring methods, optodes are much easier to operate. A major benefit of optode systems in general, is that there is limited need for recalibration, unlike electrode systems. In addition, there are no electrode solutions (or other replaceable components) or titrations required. Once the sensor is set-up, it can be left with little monitoring except to download the data periodically for verification that no drift or unexpected interference is occurring. However, light interference can limit operability. Protection from external light interference can make operability more difficult because the experiment must be designed to prevent ambient light exposure to the sample during measurement.

4.1.4 Considerations and Suggested Improvements

A few factors should be considered prior to use of the MuFO sensor. Some factors, such as the susceptibility of the sensor tip to physical damage, the phases measured, and biofouling, depend on the sampling environment. Other suggested considerations are improvements that can be made to the system, including the calibration method and temperature compensation.

The ruggedness of the sensor tip is important to consider together with the intended sample (*e.g.* fine sediments or coarse grains that can scratch the tip). An additional coating over the sensing film, such as the silicone-based layer used by Larsen *et al.* (2011), may help to protect the sensor in abrasive materials, but would decrease sensor response time.

The MuFO system, like other optical, luminescent-based methods, measures molecular oxygen, which is beneficial in that it can be used to monitor O_2 in the gaseous phase and the O_2 dissolved in water. As a result, at the time of measurement it is not discernable whether the O_2 is in the air-filled pore space or dissolved in the pore water. However, the phase can be estimated with the knowledge of the differing amount of O_2 expected in water versus air considering, for instance, that the Henry's law constant (applicable for ideal gas and incompressible fluid) is 0.032 (-) for the ratio between the aqueous/dissolved and gaseous concentrations of O_2 at equilibrium (Sander, 2014). This shows that there is 0.032 times the amount of O_2 dissolved in the pore water compared to the presence in the air of the same

pore-space. This concentration difference can be monitored to indicate whether the sensed oxygen is most likely in water or in air and indeed, O_2 has been used in the past as a proxy for water saturation in the soil environment (Ouyang, 1990).

Although not a focus during this study, the possibility of biofilm buildup and biofouling on the sensor tip can be a concern, depending on the sensor use and environment. However, there have been more cases reported of use of optodes to monitor O_2 in biofilms (*e.g.* Glud *et al.*, 1998; Kühl *et al.*, 2007; Ganesh and Radhakrishnan, 2008; and Staal *et al.*, 2011) than reports found of it as interference. Where there has been interference, the biofouling was a result of biofilm production clogging the pore system (Dutta *et al.*, 2015), which can result in reduced hydraulic permeability (Baveye *et al.*, 1998), rather than having an isolated effect on the sensor itself.

Another area for improvement is in the calibration method. The calibration method used here relied on correlating the intensity measured by the MuFO sensor to the oxygen measured by the DO probe. Thus, the error in the calibration was directly dependent on the sensitivity and error of the DO probe (mentioned in Chapter 2). An improvement would be to use a gas mixer (although the expense would eliminate advantage of affordability of the MuFO system) or gas standards for the calibration and use the DO probe for added verification of the gas concentration. This would also allow a wider range of temperature measurements since the system would not be limited to the operational range of the DO probe (down to -5 °C), which was exceeded slightly in this calibration (down to -10 °C).

The approach for correcting temperature impacts on the MuFO sensor reading can also be improved. In the FTC experiment, temperature was corrected based on the temperature readings from the probes closest to each MuFO sensor. However, this consistently resulted in differences in timing of the temperature effect noticed in the sensor reading versus actual change in temperature measured by the probes and would have skewed the data if not adjusted to match the appropriate timing. To improve this, a temperature sensitive luminophore such as Ru-phen (Koese *et al.*, 2001), europium (III) (Borisvo and Wolfbeis, 2006), or 5(6)-carboxyfluorescien (Chu and Lin, 2014) can be added to the MuFO sensing

film for direct temperature monitoring or compensation. Otherwise the temperature probes should be placed as close as possible to each MuFO sensor location.

This MuFO system is fairly basic and best suited to use in a large O_2 range where finer, trace O_2 measurements are not required. The system is easy to customize and simple to operate for laboratory experiments with varying soil moisture and temperature conditions. In general, optode systems are more versatile (can measure gaseous and dissolved O_2 in various environmental settings) and have better operability (*e.g.* less frequent recalibration) over traditional O_2 measurement methods. The main advantage of this MuFO system over commercial optode systems is the affordability, which makes this option a very competitive alternative. Overall, the MuFO system developed here served the intended purpose and is recommended for future use.

4.2 Water Table Fluctuations

The MuFO system was clearly able to show the expected fluctuation in O_2 as anticipated based on the difference in the gas diffusion and solubility in water versus air. As shown in Chapter 3, the O_2 levels followed the same trend over time of increasing with decreasing soil moisture and decreasing as moisture increased, inversely following the water table level. This trend has been seen in previous studies (*e.g.* Turcu *et al*, 2005; Haberer *et al*., 2010; Haberer *et al.*, 2011; Jost *et al.*, 2014; Dutta *et al.*, 2015). As the water entered and exited the soil column from the bottom, the lower half of the column was saturated for longer periods than the upper portion. This was reflected by the sequential response of the MuFO sensors. The sensor at -27.5 cm was the first to decrease in O_2 (followed by the point at -12.5 cm then at -6.5 cm) and last to increase (after -6.5 cm and -12.5 cm) during water table increases and decreases, respectively. There was also a clear difference in the times taken for the O_2 levels to change between maximum to minimum levels, particularly during the water table saturation process (*i.e.* oxygen decrease). The slope (Figure 13) is steepest at -6.5 cm followed by -12.5 cm and then -27.5 cm. The rate of O_2 increase was much faster than the rate of O_2 decrease. This may be explained by the differing flow rates, as previously mentioned.

Although, the difference in the dissolved and gaseous O_2 phases could not be discerned here, the variation in flow rate does impact the partitioning of O_2 between these phases. For example, Haberer *et al.* (2011) found that slow water table fluctuations resulted in a doubling of the amount of oxygen transferred through the capillary fringe into the groundwater compared to rapid changes in the water table level. This may be important to consider for future investigation on improving the optode system analysis to separate signals from gaseous and dissolved oxygen in multiphase environments.

The difference between each sensor (lower rates with increasing depths) is more likely a result of differences in physical parameters of the soil at the specific sensor location. For instance, the pore size may be slightly larger near the top of the column compared to the bottom, where compaction due to the weight of the soil (and water) above can decrease pore size. More rapid gas diffusion can occur if the pores are larger (*e.g.* macropores) compared to smaller pores (Horn and Smucker, 2005; Neira *et al.*, 2015). This is not unreasonable in this case since, following an initial soil saturation and drainage test (prior to the experiments), the soil surface level decreased by 3 cm from the initial level.

The CO_2 flux (F_{CO2}) measured from the WT experiment over time is presented in Figure 15. The much larger variations of F_{CO2} are clearly related to the water table fluctuations, with higher CO_2 fluxes coinciding with periods of water table drawdown. Following the initial CO_2 emission at the start of the experiment, the highest F_{CO2} value occurred during the lowering of the water table (up to 0.5 μmol m^{-2} s^{-1}), while subsequent F_{CO2} maxima rapidly declined in magnitude (≤0.03 μmol m^{-2} s^{-1}) when the water table rose. Water table fluctuations affect F_{CO2} because of the accompanying changes in O_2 availability and water saturation. As the water table dropped, O_2 diffused deeper into the soil column, stimulating the mineralization of organic carbon to CO_2 by soil microorganisms (Chimner and Cooper, 2003; Rezanezhad *et al.*, 2014). While the low resolution of data points in the CO_2 data cannot show if the CO_2 responded to the changes in the oxygen during the increasing water table compared to the water table decrease (rapid change in O_2), the general connection between the gas dynamics are nevertheless captured.

The oxygen concentration data (Figures 13 and 14) indicate that the soil column was predominantly anoxic with increasing water table levels. The O_2 diffusion decreased under saturated conditions since diffusion through water-filled pore space is lower than air-filled pore space. In this case, it would be expected that anaerobic respiration would be dominant and, although CO_2 was still produced, the lower diffusion through the pore space may partially explain the CO_2 flux observed (≤0.03 μmol m^{-2} s^{-1}) under water saturation. Incomplete mineralisation of the organic carbon (needed for respiration) and possible low levels of fermentation (producing CO_2) are also possible explanations for the flux observed.

With successive water table saturation-drainage cycles the oxygen consumed during respiration processes in the soil column was replenished from the atmosphere, so while it was at 0 % during saturation, it returned to consistent maximum levels (*e.g.* up to 80 % at -6.5 cm) following water table decreases for the duration of the experiment. Conversely, the CO_2 efflux fell within a fairly narrow range, 0.5 to 0.2 μmol m^{-2} s^{-1}, and exhibited a decreasing trend with time (Figure 15). This can be explained by a decreasing availability of labile organic substrates and of the accessible organic carbon pool in the soil because the original carbon source was not replenished during the experiment. Such depletion of labile organic carbon is commonly seen in reactor and soil column experiments (*e.g.*, Parsons *et al.*, 2013; Moore and Dalva, 1993). It is possible that the fluctuation of the water table promoted quicker depletion of the carbon source since, as shown by Rezanezhad *et al.* (2014), fluctuations in the water table can stimulate microbial activity. Provided adequate nutrient supply, water table fluctuation can stimulate microbial activity (for aerobic and facultative anaerobic bacteria) in the transition zone between unsaturated and saturated regions (Jost *et al.*, 2014).

In general it is seen that the higher flux of CO_2 in the headspace occurs with higher oxygen levels throughout the soil column. This is expected since a lowering of the water table would increase gas transport for oxygen and CO_2 deeper into the soil column and promote soil respiration as more favourable water content and oxygen levels occur (Chimner *et al.*, 2003). The wetting (saturated) cycle showed little difference from the previous wetting cycle oxygen values and a lower CO_2 efflux. This was anticipated because the increase in water

table up through the soil column would limit diffusion of oxygen to progressively greater soil depths (Clymo, 1983) and result in decreased aerobic respiration overall. Over time, the pattern of the oxygen changes with fluctuations of the water table were repeated at each cycle.

Overall, the expectation was met that the O_2 levels as measured by the MuFO system in the soil column and the CO_2 efflux from the soil column both increased and decreased with respective decrease and increase of the water table. For both O_2 and CO_2 this can be attributed to the physical changes and microbial activity induced by the increase/decrease in soil moisture.

4.3 Freeze-Thaw Cycles

Temperature dynamics affect many aspects of the O_2 and CO_2 gas levels in the soil because temperature influences absolute gas concentrations (including water vapour), the soil structure, the phases of pore water, and microbial activity (Marion, 1995; Smith *et al.*, 2003; Hayashi, 2013; Tucker, 2014). These factors can be interrelated. For example, as the soil temperature drops to -10 °C, most of the liquid pore water will freeze into ice (Marion, 1995), which would decrease the film of liquid water needed for substrate transport by microorganisms performing respiration. In addition, since water expands when freezing, the volume of the air-filled pore space would shrink, thereby decreasing gas diffusion (Tucker, 2014), while the total solid phase component would increase. Another example is that, while some liquid water will be drawn toward the frozen front by thermo-osmosis (Biermans *et al*., 1978), portions of water can remain unfrozen under sub-zero conditions and form thin films on soil particles, enabling water and solute movement (Marion, 1995) and facilitating microbial activity. The range, frequency, and duration of the imposed temperature dynamics also influence the gas dynamics and affect the microbial community (Henry, 2007).

The experimental set-up here had multiple physical conditions at play. The unsaturated zone was exposed to freezing, whereas the saturated zone experienced limited temperature fluctuations in between +4 °C and +10 °C (Appendix A6). This is important to consider because, had the entire column been saturated, the freezing zone would be expected to have

posed a greater physical barrier to gas transport as there would have been more water available for ice lens development and likely the formation of a complete seal in the top layer of the column. Additionally, waterlogged soils would promote anaerobic respiration and little oxygen would be expected to be found at more than a few centimeters below the soil surface (Drew and Lynch, 1980). In contrast, had the entire column been unsaturated, the extent of ice formation would be lower and any ice formed would be limited in preventing gas exchange between the soil and the atmosphere. Thus, the higher oxygen concentrations would be expected to be found at greater depths compared to the fully and partially saturated column set-ups under the same temperature regime.

Figure 16 shows the depth profiles of oxygen saturation in the soil column under a freeze-thaw cycle. The oxygen measurements indicate a decrease in oxygen levels during freezing conditions relative to the thawing conditions. This is in line with other studies such as that by de Bruijn *et al.* (2009), who found the oxygen diffusion into soils is reduced by freeze-thaw processes, thus promoting anaerobic processes (*e.g.* denitrification and anaerobisis). However, while oxygen (and CO_2) decreased during the frozen periods to levels lower than in the thaw periods, it was never completely absent at the points monitored near and above the water table. This indicates that aerobic respiration would still have been possible at these levels. In addition, the temperature variation near the water table would have been lower than in the unsaturated zone nearer to the soil surface as residual heat from the band heater kept the -10 cm and -7 cm locations above zero degrees centigrade. This would be a more favourable zone for microbes and may be a hotspot for microbial communities. While monitoring of microbial presence and activity was not done here, it could give valuable insight into the system as a whole and is recommended in future work.

As expected, only the upper portion of the soil was affected by FTCs, while the conditions below the water table remained constant in terms of groundwater temperature and oxygen saturation. The point at -1 cm was close to the atmosphere so the oxygen levels during the frozen periods and the thawed periods were constant. However, the oxygen measured was still lower under the frozen condition compared to the thawed condition. This may be explained by the fact that the port to the humid air, which was supplied to the headspace,

had to be closed during the frozen period because ice would form in the tubing and block the air flow causing pressure build-up in the line. However, the headspace was still open to the environmental chamber atmosphere through a top port, so the air could be replenished at a constant rate, but in lower amounts. This effect is also seen in the lower depths at -7 cm and at -10 cm. More specifically, following the ideal gas law, the decrease in O_2 with decreasing temperature can be explained by a proportional decrease in the volume of air-filled pore-space (due to ice build-up and upward movement of liquid water). Another possibility is a decrease in pressure instead of, or in conjunction with, the decrease in volume. However, neither pressure nor pore water were monitored, so the factors balancing the oxygen and temperature decreases cannot be conclusively attributed to one or both of these conditions.

The area just above and below the water table (-7 cm and -10 cm) was interesting in that there was a decrease oxygen concentration during the thaw period, which is indicative of an increase in aerobic respiration relative to the frozen period where the oxygen levels did not vary. As the most energetically favourable TEA, oxygen would have been consumed quickly, outpacing resupply from the atmosphere. During the frozen period the sensors at -7 cm and -10 cm showed unchanging levels of oxygen. This was likely due to a combination of lower microbial activity and decreased infiltration of atmospheric oxygen due to any changes in soil structure and pore networks (possibly due to ice blockage) with the onset of the frozen period. It was also found here, that a key factor affecting gas diffusion during freezing of unsaturated systems is the physical change in soil pathways for gas movement. For instance, during the MuFO calibration, certain sensor locations in the soil (Appendix A2) did not respond to changes in the gas sparging between oxygen and nitrogen until the soil was frozen below zero degrees centigrade. This indicates that the freezing process can itself influence the physical soil properties (assumed to be by ice blockage and, to an extent, grain rearrangement) of the soil and thus the oxygen dynamics by opening or closing pathways to the atmosphere. Such structural changes exert a strong influence on diffusion and hence oxygen transport in porous media (Neira *et al.*, 2015).

The lower portion of the soil column was completely saturated with water and therefore anoxic. Additionally, the band heater prevented temperature fluctuations in this lower water

saturated zone, so no response to the FTCs was anticipated or observed. Any initial oxygen in this zone was rapidly consumed before the environment became exclusive to anaerobic respiration pathways (*e.g.,* denitrification, sulfate reduction).

The oxygen dynamics in soil due to FTCs affected the CO_2 efflux (F_{CO2}). The F_{CO2} measured in the headspace of the soil column is shown in Figure 18. In each FTC, the flux of CO_2 was notably lower (<0.05 μmol m^{-2} s^{-1}) during frozen periods relative to the thaw periods. However, there was still a measureable efflux of CO_2, similar to the seen by Kurganova *et al.* (2007), which likely indicates that the conditions were not completely anoxic, but may also have been caused by metabolism of other electron acceptors in the soil column. As the soil thawed, any physical barriers (ice) were removed allowing O_2 to diffuse into the soil, hence stimulating the mineralization of organic carbon to CO_2 by soil microorganisms. An important point to clarify here is that the soil respiration measured in this study was strictly heterotrophic; autotrophic respiration, such as from plant metabolism (Högberg *et al.,* 2001), was not incorporated into this study, but is recognized as an important source of CO_2.

During the first thaw condition, a high F_{CO2} (12 μmol m^{-2} s^{-1}) was measured, while subsequent F_{CO2} rapidly declined when the soil froze. F_{CO2} in the headspace of the column exhibited periodic variations by FTCs, with peak values during soil thaw periods. A pulse of CO_2 emitted from the soil at the start of each thaw event, as seen in this experiment, has been observed in many other freeze-thaw experiments. Matzner and Borken (2008) summarized the results of 15 such studies and found that CO_2 pulses upon thawing were seen in 10 of the studies (both field and laboratory scales), with freezing periods ranging from 6 hours to 3 months. Additionally, Kurganoza *et al.* (2007), observed pulses of CO_2 with the onset of thawing and ongoing (though very low) CO_2 efflux was seen during frozen periods. These were attributed to a combination of: physical release of gas previously trapped, ongoing biological activity in the unfrozen water films that were on the surface of the soil particles, increase in substrate availability with microbial death upon freezing, and the respiration by microbes adapted to the colder temperature. These CO_2 pulses exhibited a progressive

attenuation in successive FTCs (see Figure 18). The results of the CO_2 flux from the soil column during FTCs can support the hypothesis that under frozen conditions, the oxygen concentrations decrease due to a combination of changes in the pore network and the oxygen consumption.

Overall the expected results were achieved. For the unsaturated zone, it was initially hypothesized that the pore water would freeze where the temperature was below zero degrees centigrade, resulting in a decrease of air-filled pore volume in the unsaturated zone. Consequently, the volume for gas diffusion in air would be limited, or else completely blocked by ice build-up in the top of the soil layer. The measured O_2 in the soil column (unsaturated zone) was expected to decrease in sub-zero conditions with increasingly limited replenishment to lower regions of the column. In addition, the emission of temperature sensitive microbial respiration products (CO_2) was expected to decrease under the lower temperature. During the thaw period, it was expected that the CO_2 efflux would increase as air-filled pore space increased with the reopening of gas diffusion channels and as aerobic respiration restarted and microbial activity increased in response to warmer temperatures. Similarly, the O_2 levels in the unsaturated zone were predicted to increase with replenishment from the atmosphere as diffusion ability increased. The changes in O_2 in response to temperature in the saturated and unsaturated zones were captured with the MuFO system and were largely in agreement with the expected changes in oxygen dynamics.

CHAPTER 5: CONCLUSION

In this study, a *Multi-Fibre Optode* sensing method was developed and tested as a tool for obtaining high temporal resolution measurements of O_2 in soil environments. The MuFO sensor was evaluated against a selection of commercially available optodes on the basis of affordability, technical specifications, and operability. The system was tested in two soil column experiments where dynamic shifts in O_2 levels are known or most likely to occur as a result of the imposed environmental conditions. CO_2 data was used as verification of gas diffusion and ongoing soil respiration under the imposed hydrologic and temperature regimes.

In the first column experiment, temporal change in O_2 was examined with changing soil water content, with the aim of testing the ability of the MuFO system to broadly distinguish the variation of O_2 levels between saturated and unsaturated zones. As gas diffusion in air is on the order of 10^4 times that of diffusion in water, it was anticipated that the oxygen levels detected would be much lower under saturated conditions compared to unsaturated conditions along with the CO_2, ultimately due to limited diffusion ability. The expectation was met as the O_2 levels (measured by the MuFO system in the soil column) and the CO_2 efflux from the soil column both increased and decreased with respective decrease and increase of the water table. For both O_2 and CO_2, this can be attributed to the physical changes and microbial activity (affecting O_2 consumption and CO_2 production) induced by the increase/decrease in soil moisture. The CO_2 efflux appeared to follow the water table closely with an inverse relationship, but the maximum efflux at each cycle decreased in magnitude over time, as the organic carbon pool was depleted.

The O_2 readings at each point responded in the expected sequence as the water table passed each point. However, the rate of decrease in O_2 increased with proximity to the soil surface, which means that there may have been a physical difference in the soil at each depth (*e.g.* decreasing gas diffusion ability due to compaction from loading). The data also showed the rates of oxygen depletion (with water table increase) to be lower than the rates of

replenishment (with water table decrease), which indicates that the imposed water table fluctuation was not completely constant over time.

The second column experiment was more complex as it was designed to examine the O_2 distributions in soils (saturated and unsaturated) under cycles of freezing and thawing. These FTCs were imposed on the soil column through controlled variation of surface air temperature between -10 °C and +10 °C. To our knowledge, no soil studies on freezing and thawing processes have included O_2 monitoring within a soil profile, which makes this research novel in that regard.

For the freeze-thaw experiment it was hypothesized that, under frozen conditions, the pore water would freeze where the temperature was below zero degrees centigrade, decreasing the air-filled pore volume in the unsaturated zone starting from the soil surface. As a result, the volume for gas diffusion was expected to decrease and the measured O_2 in the unsaturated zone would drop during sub-zero conditions with increasingly limited physical replenishment of O_2 to lower regions of the column. In addition, the emission of temperature-sensitive microbial respiration products (CO_2) was expected to decrease under the lower temperature. During the thaw period, it was expected that the CO_2 efflux would increase as air-filled pore space increased with the reopening of gas diffusion channels and as aerobic respiration restarted and microbial activity increased in response to warmer temperatures. Similarly, the O_2 levels in the unsaturated zone were predicted to increase with replenishment from the atmosphere as diffusion ability increased.

Overall, the changes in O_2 in response to temperature in the saturated and unsaturated zones were captured successfully with the MuFO system and were largely in agreement with the expected changes in oxygen dynamics. The sensors in the saturated zone showed no change in oxygen for the duration of the FTC experiment, which can be explained by the fact that the lower region of the column did not fluctuate with temperature and was anoxic due the waterlogged condition. The unsaturated zone showed higher levels of O_2 under thawed conditions compared to frozen conditions. This can be explained by a combination of decreased air flow in the headspace in addition to lower air-filled pore-space as the freezing of the liquid water would increase the total solid phase (soil particles plus ice). The lower

temperature also decreased the CO_2 efflux, which might be explained by the physical limits on gas diffusion, less oxygen available for aerobic respiration, and the lower temperature reducing microbial activity.

During the thawing period, the oxygen increased quickly as the physical ice barriers melted enabling gas flow in the headspace and diffusion in the soil column. At the monitoring points just above and below the water table, the levels soon began to decline, likely indicating increased microbial activity (as oxygen is used in aerobic respiration) with the warming temperature. Similarly, the CO_2 pulse in efflux at the onset of thawing, which supports the idea of the physical barrier removal allowing gas exchange to resume. Following the pulse, the CO_2 decreased again, but was still much greater than under frozen conditions, indicating greater microbial activity as the likely cause. The CO_2 emission was still present under frozen conditions, which shows that the ice did not completely seal off the soil from the headspace and that microbial activity was ongoing, but at low levels. As in the WT experiment, the magnitude of the pulse of CO_2 efflux diminished with successive FTCs as the organic carbon source became depleted.

The MuFO system works on an optical luminescence basis, so it does not consume oxygen and is fully reversible. It can be customized in design to meet the specific spatial and temporal measurement needs of the user for a given study. Therefore, it is ideal for collection of real-time O_2 data over a short or long term. This MuFO system faired moderately well in comparison to the commercially available systems. It is weaker with respect to technical specifications, but is nevertheless well suited for use in soil experiments, particularly where measurement of a large oxygen range of oxygen levels is required. The strongest advantage of the MuFO system over commercial sensors is the low price for manufacture and operation. Additionally, this system is easy to customize and simple to operate for laboratory experiments with varying soil moisture and temperature. The MuFO system is also advantageous over traditional O_2 measurement methods (such as the Clark electrode and Winkler titration) in that it is more versatile and easier to use once installed. Overall, the MuFO system developed here is recommended for future use in molecular oxygen monitoring.

It can be concluded that the MuFO system has been successfully implemented in two bench-scale experiments under varying hydrological and temperature regimes. The implications of the successful use of this system are that it has been proven to work well in a controlled soil environment and can be useful in future investigations to improve the understanding of the biogeochemical surface and subsurface processes in different environments, ranging from terrestrial to aquatic settings. The system can provide information about the redox environment, microbial activity, and physical changes in the environment. It can therefore be useful in many applications such as: investigation of the role of soil respiration processes on climate change, monitoring bioremediation of contaminated sites, or evaluation of constructed wetland performance.

With the aim of addressing research needs at the field scale, the next steps in development of the MuFO system are modification and testing for field studies. As of this writing, the Ecohydrology Research Group at the University of Waterloo (where this MuFO system was developed) is working in collaboration with Hoskin Scientific Ltd., with financial support through an NSERC Engage grant, to incorporate the MuFO technology into an autonomous, field-deployable system with "photo-logging" capability. The addition of data telemetry capabilities will allow for continuous and remote monitoring of O_2 concentrations in surface and subsurface environments in real-time. A prototype portable MuFO system has been constructed and will be deployed in extensive field trials in the spring. With this enhancement, the MuFO system can be incorporated into a larger variety of studies at the laboratory and field scales, so that a more complete understanding of oxygen dynamics can be gained and used in providing a complete picture of the biogeochemical processes of concern today and in the future.

REFERENCES

Aerts, R., and Ludwig, F. (1997). Water-table changes and nutritional status affect trace gas emissions from laboratory columns of peatland soils. *Soil Biology and Biochemistry*, 29, 1691–1698.

Amao, Y. (2003). Probes and Polymers for Optical Sensing of Oxygen. *Microchimica Acta*, 143, 1–12.

Angert, A., Yakir, D., Rodeghiero, M., Preisler, Y., Davidson, E. A., and Weiner, T. (2015). Using O_2 to study the relationships between soil CO_2 efflux and soil respiration. *Biogeosciences*, 12, 2089–2099.

Apostol, I., Miller, K. J., Ratto, J., and Kelner, D. N. (2009). Comparison of different approaches for evaluation of the detection and quantitation limits of a purity method: A case study using a capillary isoelectrofocusing method for a monoclonal antibody. *Analytical Biochemistry*, 385, 101–106.

Badocco, D., Mondin, A., Fusar, A., Favaro, G., and Pastore, P. (2009a). Influence of the real background signal on the linearity of the Stern-Volmer calibration for the determination of molecular oxygen with optical sensors. *Journal of Physical Chemistry C*, 113, 15742–15750.

Badocco, D., Mondin, A., Fusar, A., and Pastore, P. (2009b). Calibration Models under Dynamic Conditions for Determining Molecular Oxygen with Embedded in Polymeric Matrixes. *J. Phys. Chem. C*, (model III), 20467–20475.

Badocco, D., Mondin, A., and Pastore, P. (2012). Determination of thermodynamic parameters from light intensity signals obtained from oxygen optical sensors. *Sensors and Actuators, B: Chemical*, 163, 165–170.

Badocco, D., Mondin, A., and Pastore, P. (2013a). Signal drift of oxygen optical sensors. Part I: Rationalization of the drift nature and its experimental check with a light intensity detection based sensor. *Sensors and Actuators, B: Chemical*, 181, 943–948.

Badocco, D., Mondin, A., and Pastore, P. (2013b). Signal drift of oxygen optical sensors. Part II: "Smart" drift correction algorithm and its experimental check with a light intensity detection based sensor. *Sensors and Actuators, B: Chemical*, 181, 949–954.

Bagshaw, E. A, Wadham, J. L., Mowlem, M., Tranter, M., Eveness, J., Fountain, a G., and Telling, J. (2011). Determination of dissolved oxygen in the cryosphere: a comprehensive laboratory and field evaluation of fiber optic sensors. *Environmental Science and Technology*, 45, 700–5.

Baveye, P., Vandevivere, P., Hoyle, B. L., DeLeo, P. C., and de Lozada, D. S. (1998). Environmental Impact and Mechanisms of the Biological Clogging of Saturated Soils and Aquifer Materials. *Critical Reviews in Environmental Science and Technology*, 28, 123–191.

Beneš, M., Krupič, L., and Štefan, R., (2015). On coupled heat transport and water flow in partially frozen variably saturated porous media. Applied Mathematical Modelling, 29, 6580-6598.

Benson, B. B., and Krause, D. (1980). The concentration and isotopic fractionation of gases dissolved in freshwater in equilibrium with the atmosphere. 1. Oxygen *Limnology and Oceanography*, *25*, 662–671.

Benson, B. B., and Krause, D. (1984). The concentration and isotopic fractionation of oxygen dissolved in freshwater and seawater in equilibrium with the atmosphere. *Limnology and Oceanography*, 29, 620–632.

Biermans, M. B. G. M., Dijkema, K. M., and Vries, D. A. D. E. (1978). Water movement in porous media towards and ice front. *Journal of Hydrology*, 37, 137–148.

Blodau, C. and Moore, T. R. (2003). Experimental response of peatland carbon dynamics to a water table fluctuation. *Aquatic Sciences*, 65, 47–62.

Blossfeld, S., Gansert, D., Thiele, B., Kuhn, A. J., and Lösch, R. (2011). The dynamics of oxygen concentration, pH value, and organic acids in the rhizosphere of Juncus spp. *Soil Biology and Biochemistry*, 43, 1186–1197.

Borisov, S.M., Wolfbeis, O.S. (2006). Temperature-sensitive europium (III) probes and their use for simultaneous luminescent sensing of temperature and oxygen, Anal. Chem. 78, 5094–5101.

de Bruijn, A. M. G., Butterbach-Bahl, K., Blagodatsky, S., and Grote, R. (2009). Model evaluation of different mechanisms driving freeze-thaw N_2O emissions. *Agriculture, Ecosystems and Environment*, 133, 196–207.

Bunting, B. T. (1965). The Geography of Soil. London: Hutchinson & Co. Chapter 5.

Carpenter, J. H. (1965). Measurements in Pure and of Oxygen Solubility. *Limnology and Oceanography*, 10, 135–140.

Carritt, D. E. and Kanwisher, J. W. (1959). An electrode system for measuring dissolved oxygen. *Analytical Chemistry*, 31, 5–9.

Chen, R., Mcpeak, H., Formenti, F., Hahn, C., Farmery, A., Obeid, A., and Park, M. (2013). Optimizing sensor design for polymer fibre optic oxygen sensors. *Sensors 2013 IEEE*, 13–16. DOI: 10.1109/ICSENS.2013.6688294.

Chimner, R. A., and Cooper, D. J. (2003). Influence of water table levels on CO_2 emissions in a Colorado subalpine fen: An in situ microcosm study. *Soil Biology and Biochemistry*, 35, 345–351.

Chu, C. S., and Lin, C. A. (2014). Optical fiber sensor for dual sensing of temperature and oxygen based on PtTFPP/CF embedded in sol-gel matrix. *Sensors and Actuators, B: Chemical*, 195, 259–265.

Clark, C. M., Hancke, K., Xydes, A., Hall, K., Schreiber, F., Klemme, J., and Moline, M. (2013). Estimation of volumetric oxygen concentration in a marine environment with an autonomous underwater vehicle. *Journal of Field Robotics*, 30, 1–16.

Clymo, R.S., (1983). Peat. In: Ecosystems of the World, 4A. Mires: swamp, bog, fen and moor, General Studies, Elsevier, Amsterdam, p. 159–224.

Cussler, E. L. (1997). Diffusion: Mass Transfer in Fluid Systems (2nd edition). New York: Cambridge University Press.

Diogo, H. P., and Ramos, J. J. M. (2012). Slow molecular mobility in the amorphous thermoplastic polysulfone: A TSDC investigation. *Journal of Thermal Analysis and Calorimetry*, 111, 773–779.

Drew, M. C., and Lynch, J. M. (1980). Soil Anaerobiosis, Microorganisms, and Root Function. *Annual Review of Phytopathology*, 18, 37–66.

Dutta, T., Carles-Brangarí, A., Fernàndez-Garcia, D., Rubol, S., Tirado-Conde, J., and Sanchez-Vila, X. (2015). Vadose zone oxygen (O_2) dynamics during drying and wetting cycles: An artificial recharge laboratory experiment. *Journal of Hydrology*, 527, 151–159.

Elberling, B., Askaer, L., Jørgensen, C. J., Joensen, H. P., Kühl, M. C., Glud, R. N., and Lauritsen, F. R. (2011). Linking soil O_2, CO_2, and CH_4 concentrations in a wetland soil: Implications for CO_2 and CH_4 fluxes. *Environmental Science and Technology*, 45, 3393–3399.

Fetter, C. (2001). *Applied hydrogeology* (4th ed.). Upper Saddle River, N.J.: Prentice Hall.

Fischer, J. P. and Koop-Jakobsen, K. (2012). The multi fiber optode (MuFO): A novel system for simultaneous analysis of multiple fiber optic oxygen sensors. *Sensors and Actuators, B: Chemical*, 168, 354–359.

Ganesh, A. B., and Radhakrishnan, T. K. (2008). Fiber-optic sensors for the estimation of oxygen gradients within biofilms on metals. *Optics and Lasers in Engineering*, 46, 321–327.

Geethanjali, H. S., Nagaraja, D., Melavanki, R. M., and Kusanur, R. A. (2015). Fluorescence quenching of boronic acid derivatives by aniline in alcohols – A Negative deviation from Stern–Volmer equation. *Journal of Luminescence*, 167, 216–221.

Glud, R. N., Santegoeds, C. M., De Beer, D., Kohls, O., and Ramsing, N. B. (1998). Oxygen dynamics at the base of a biofilm studied with planar optodes. *Aquatic Microbial Ecology*, 14, 223–233.

Glud, R. N. (2008). Oxygen dynamics of marine sediments. *Marine Biology Research*, 4, 243–289.

Grogan, P., Michelsen, A., Ambus, P. and Jonasson, S. (2004). Freeze-thaw regime effects on carbon and nitrogen dynamics in sub-arctic heath tundra mesocosms. *Soil Biolology and Biochemistry*, 36, 641-654.

Haberer, C. M., Rolle, M., Liu, S., Cirpka, O. A, and Grathwohl, P. (2011). A high-resolution non-invasive approach to quantify oxygen transport across the capillary fringe and within the underlying groundwater. *Journal of Contaminant Hydrology*, 122, 26–39.

Hammer, D. A. (editor. (1989). Constructed Wetlands for Wastewater Treatment: Municipal, Industrial, and Agricultural. Lewis publishers, Florida.

Hasumoto, H., Imazu, T., Miura, T., and Kogure, K. (2006). Use of an optical oxygen sensor to measure dissolved oxygen in seawater. *Journal of Oceanography*, 62, 99–103.

Hayashi, M. (2013). The cold vadose zone: Hydrological and ecological significance of frozen-soil processes. *Vadose Zone Journal*. 12. doi:10.2136/vzj2013.03.0064

Hefting, M. M., Clément, J.C., Dowrick, D., Cosandey, A. C., Bernal, S., Cimpian, C., Pinay, G. (2004). Water table elevations controls on soil nitrogen cycling in riparian wetlands along a European climatic gradient. *Biogeochemistry*, 67, 113–134.

Helm, I., Jalukse, L., and Leito, I. (2012). A highly accurate method for determination of dissolved oxygen: Gravimetric Winkler method. *Analytica Chimica Acta*, 741, 21–31.

Henry, H. A. L. (2007). Soil freeze-thaw cycle experiments: Trends, methodological weaknesses and suggested improvements. *Soil Biology and Biochemistry*, 39, 977–986.

Hentschel, K., W. Borken and E. Matzner. (2008). Repeated freeze–thaw events affect leaching losses of nitrogen and dissolved organic matter in a forest soil. *Journal of Plant Nutrition and Soil Science,* 171, 699-706.

Högberg P., Nordgren A., Buchmann N., Taylor A.F.S., Ekblad A., Hogberg M.N., Nyberg G., Ottosson-Lofvenius M. and Read D.J. (2001). Large-scale forest girdling shows that current photosynthesis drives soil respiration. Nature 411: 789–792.

Horn, R., and Smucker, A. (2005). Structure formation and its consequences for gas and water transport in unsaturated arable and forest soils. *Soil and Tillage Research*, 82, 5–14.

Huesemann, M. H., and Truex, M. J. (1996). The role of oxygen diffusion in passive bioremediation of petroleum contaminated soils. *Journal of Hazardous Materials*, 51, 93–113.

International Conference on Harmonization, Harmonized tripartite guideline Q2R1, Validation of analytical procedures, ICH Q2R1, 1–13, 2005.

Jonasson, S., Michelsen, A., and Schmidt, I.K. (1999). Coupling of nutrient cycling and carbon dynamics in the Arctic, integration of soil microbial and plant processes. *Applied Soil Ecology,* 11, 135-146.

Joseph, G. and Henry, H.A.L. (2008). Soil nitrogen leaching losses in response to freeze-thaw cycles and pulsed warming in a temperate old field. *Soil Biolology and Biochemistry*. 40, 1947-1953.

Jost, D., Haberer, C. M., Grathwohl, P., Winter, J., and Gallert, C. (2014). Oxygen Transfer in a Fluctuating Capillary Fringe: Impact of Microbial Respiratory Activity. *Vadose Zone Journal,* 14. doi:10.2136/vzj2014.04.0039

Kangas, P. C. (2004). Ecological Engineering Principles and Practice. Lewis Publishers, Florida. p. 25-68.

Kautsky, H., (1937). Quenching of Luminescence by Oxygen. *Biochem. Z.*, 291, 271.

Klimant, I., and O. S. Wolfbeis. (1995). Oxygen-sensitive luminescent materials based on silicone-soluble ruthenium diimine complexes. Anal. Chem. 67, 3160–3166.

Klimant, I., Kühl, M., Glud, R. N., and Holst, G. (1997). Optical measurement of oxygen and temperature in microscale: strategies and biological applications. *Sensors and Actuators B: Chemical*, 38, 29–37.

Kocincova, A. S., Borisov, S. M., Krause, C., and Wolfbeis, O. S. (2007). Fiber-optic microsensors for simultaneous sensing of oxygen and pH, and of oxygen and temperature. *Analytical Chemistry*, 79, 8486–8493.

Koese, M.E., Carroll, B.F., Schanze K.S., (2001). Preparation and spectroscopic proper- ties of multiluminophore luminescent oxygen and temperature sensor films. *Langmuir,* 39, 9121–9129.

Kühl, M., Rickelt, L. F., and Thar, R. (2007). Combined imaging of bacteria and oxygen in biofilms. *Applied and Environmental Microbiology*, 73, 6289–6295.

Kurganova, I., Teepe, R., and Loftfield, N. (2007). Influence of freeze-thaw events on carbon dioxide emission from soils at different moisture and land use. *Carbon Balance and Management*, *2*, 2. http://doi.org/10.1186/1750-0680-2-2.

Lakowicz, Joseph R. (1999). Principles of Fluorescence Spectroscopy. Kluwer Academic/ Plenum Publishers. p. 8.

LaRowe, D.E. and Van Cappellen, P. (2011) Degradation of natural organic matter: a thermodynamic analysis. *Geochimica et Cosmochimica Acta*, 75, 2017-2236.

Larsen, M., Borisov, S. M., Grunwald, B., Klimant, I., and Glud, R. N. (2011). A simple and inexpensive high resolution color ratiometric planar optode imaging approach: application to oxygen and pH sensing. *Limnology and Oceanography: Methods*, 9, 348–360.

Lo, Y. L., Chu, C. S., Yur, J. P., and Chang, Y. C. (2008). Temperature compensation of fluorescence intensity-based fiber-optic oxygen sensors using modified Stern-Volmer model. *Sensors and Actuators, B: Chemical*, 131, 479–488.

Marion, G.M., (1995). Freeze-thaw processes and soil chemistry. U.S. Army Corps of Engineers, Cold Regions Research and Engineering Laboratory, Hanover, N.H. Special Report 95-12.

Martinez-Olmos, A., De Vargas-Sansalvador, I. M. P., Palma, A. J., Banqueri, J., Fernández-Ramos, M. D., and Capitán-Vallvey, L. F. (2011). Multisensor probe for soil monitoring. *Sensors and Actuators, B: Chemical*, 160, 52–58.

Matzner, E., and Borken, W. (2008). Do freeze-thaw events enhance C and N losses from soils of different ecosystems? A review. *European Journal of Soil Science*, 59, 274–284.

Miao, G., Noormets, A., Domec, J.-C., Trettin, C. C., McNulty, S. G., Sun, G., and King, J. S. (2013). The effect of water table fluctuation on soil respiration in a lower coastal plain forested wetland in the southeastern U.S. Journal of Geophysical Research: *Biogeosciences*, 118, 1748–1762.

Mock, T., Dieckmann, G. S., Haas, C., Krell, A., Tison, J. L., Belem, A. L., Papadimitriou, S., and Thomas, D. N. (2002). Micro-optodes in sea ice: A new approach to investigate oxygen dynamics during sea ice formation. *Aquatic Microbial Ecology*, 29, 297–306.

Moore, T. R., and Dalva, M. 1993. The influence of temperature and water table position on carbon dioxide and methane emissions from laboratory columns of peatland soils. *European Journal of Soil Science*, 44, 651–664.

Moyer, E., and Kostecki, P. (2003). MTBE remediation handbook. Amherst, MA: Amherst Scientific. p. 249.

Neira, J., Ortiz, M., Morales, L., and Acevedo, E. (2015). Oxygen diffusion in soils: Understanding the factors and processes needed for modeling, 75, 35–44.

Niederkorn, A. (2015). Surface-subsurface hydrologic exchange and nutrient dynamics in a groundwater-fed stream, Bauman Creek, Ontario, Canada. UWSpace. *http://hdl.handle.net/10012/9399.*

Norris, J.R. and Ribbons, D.W. (1969). Methods in Microbiology, Volume 3, Part 2. Academic Press. p. 122.

Ouyang, Y. (1990). Dynamic Mathematical Model of Oxygen and Carbon Dioxide Exchange between Soil and Atmosphere (Doctoral dissertation). Oregon State University.

Ouyang, Y., and Zheng, C. (2000). Surficial processes and CO_2 flux in soil ecosystem. *Journal of Hydrology*, 234, 54–70.

Parsons, C. T., Couture, R. M., Omoregie, E. O., Bardelli, F., Greneche, J. M., Roman-Ross, G., and Charlet, L. (2013). The impact of oscillating redox conditions: Arsenic immobilisation in contaminated calcareous floodplain soils. *Environmental Pollution*, 178, 254–263.

Precht, E., Franke, U., Polerecky, L., and Huettel, M. (2004). Oxygen dynamics in permeable sediments with wave-driven pore water exchange. *Limnology and Oceanography*, 49, 693–705.

Quaranta, M., Borisov, S. M., and Klimant, I. (2012). Indicators for optical oxygen sensors. *Bioanalytical Reviews*, 4, 115–157.

Rasband, W.S., (2015). ImageJ, U. S. National Institutes of Health, Bethesda, Maryland, USA, http://imagej.nih.gov/ij/, 1997-2016.

Rezanezhad, F., R.-M. Couture, R. Kovac, D. O'Connell, P. Van Cappellen. (2014). An automated fluctuating water table column system to study soil biogeochemistry under redox-dynamic conditions. *Journal of Hydrology*, 509, 245-256.

Rezanezhad, F., Price, J. S., Quinton, W. L., Lennartz, B., Milojevic, T., and Van Cappellen, P. (2016). Structure of peat soils and implications for water storage, flow and solute transport: A review update for geochemists. *Chemical Geology,* 429, *75*–84.

Rohatgi-Mukherjee, K. K. (1978). Fundamental of Photochemistry (A Halsted Press book). New York: Wiley.

Rounds, S.A., Wilde, F.D., and Ritz, G.F., (2013). Dissolved oxygen (version 3.0): U.S. Geological Survey Techniques of Water-Resources Investigations, Book 9, Chapter A6, Section 6.2, *http://water.usgs.gov/owq/FieldManual/Chapter*6/6.2_v3.0.pdf.

Sander, R. (2015). Compilation of Henry's law constants (version 4.0) for water as solvent. *Atmospheric Chemistry and Physics*, 15, 4399–4981.

Santner, J., Larsen, M., Kreuzeder, A., and Glud, R. N. (2015). Two decades of chemical imaging of solutes in sediments and soils - a review. *Analytica Chimica Acta*, 878, 9–42.

Smith, K. a., Ball, T., Conen, F., Dobbie, K. E., Massheder, J., and Rey, a. (2003). Exchange of greenhouse gases between soil and atmosphere: interactions of soil physical factors and biological processes. *European Journal of Soil Science*, 54, 779–791.

Staal, M., Prest, E. I., Vrouwenvelder, J. S., Rickelt, L. F., and Kühl, M. (2011). A simple optode based method for imaging O_2 distribution and dynamics in tap water biofilms. *Water Research*, 45, 5027–5037.

Stich, M. I. J., Borisov, S. M., Henne, U., and Schäferling, M. (2009). Read-out of multiple optical chemical sensors by means of digital color cameras. *Sensors and Actuators, B: Chemical*, 139, 204–207.

Stern, O. and Volmer, M. (1919). Sind die Abweichungen der Atomgewichte von der Ganzzahligkeit durch Isotopie erklärbar? *Physik, Z.*, 20, 183-188.

Taillefert, M., Luther, G. W., and Nuzzio, D. B. (2000). The application of electroanalytical tools for in situ measurements in aquatic systems. *Electroanalysis,* 12, 411.

Tan, K. (2000). Environmental soil science (2nd edition). New York: Marcel Dekker, Inc.

Teepe, R. and B. Ludwig. (2004). Variability of CO_2 and N_2O emissions during freeze-thaw cycles: results of model experiments on undisturbed forest-soil cores. *Journal of Plant Nutrition and Soil Science,* 167, 153-159.

Torres, E. Couture, R.M., Shafei, B., Nardi, A., Ayora, C. and Van Cappellen, P. (2015) Reactive transport modeling of early diagenesis in a reservoir lake affected by acid mine drainage: Trace metals, lake overturn, benthic fluxes and remediation. *Chemical Geology*, 419, 75-91.

Tucker, C. (2014). Reduction of air- and liquid water-filled soil pore space with freezing explains high temperature sensitivity of soil respiration below 0°C. *Soil Biology and Biochemistry*, 78, 90–96.

Turcu, V. E., Jones, S. B. and Or, D. (2005). Continuous Soil Carbon Dioxide and Oxygen Measurements and Estimation of Gradient-Based Gaseous Flux. *Vadose Zone J.*, 4, 1161–1169.

Wang, Y. and Van Cappellen, P. (1996). A multicomponent reactive transport model of early diagenesis: Application to redox cycling in coastal marine sediments. *Geochim. Cosmochim. Acta*, 60, 2993–3014

Wang, X. and Wolfbeis, O. S. (2014). Optical methods for sensing and imaging oxygen: materials, spectroscopies and applications. *Chemical Society Reviews*, 43, 3666–3761.

Winkler, L. W. (1888). Die Bestimmung des in Wasser Gelösten Sauerstoffes*. Berichte der Deutschen Chemischen Gesellschaft* 21: 2843–2855.

Wolfbeis, O. S. (2015). Luminescent sensing and imaging of oxygen: Fierce competition to the Clark electrode. *BioEssays*, 37, 921–928.

Woźniak, R., Dittmer, U., and Welker, A. (2007). Interaction of oxygen concentration and retention of pollutants in vertical flow constructed wetlands for CSO treatment. *Water Science and Technology*, 56*, 31–38.*

Yu, X., Zou, Y., Jiang, M., Lu, X., and Wang, G. (2011). Response of soil constituents to freeze-thaw cycles in wetland soil solution. *Soil Biology and Biochemistry,* 43, 1308-1320.

APPENDIX

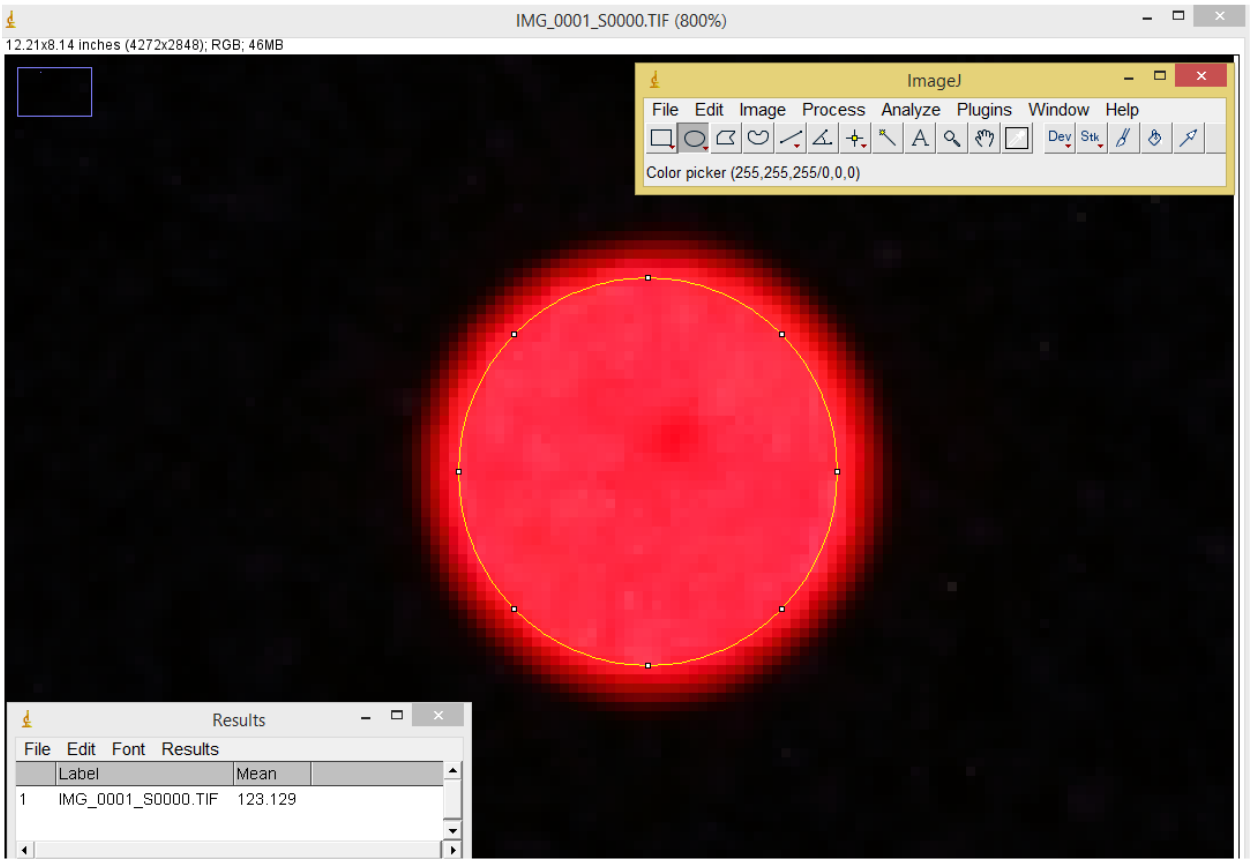

Figure A1: Example of resulting image (as tiff file prior to image processing in ImageJ program) of sensor light intensity as captured by digital camera. Area within circled region of red spot indicates region of interest (ROI) designated for use in calculation of average light intensity at the point and time.

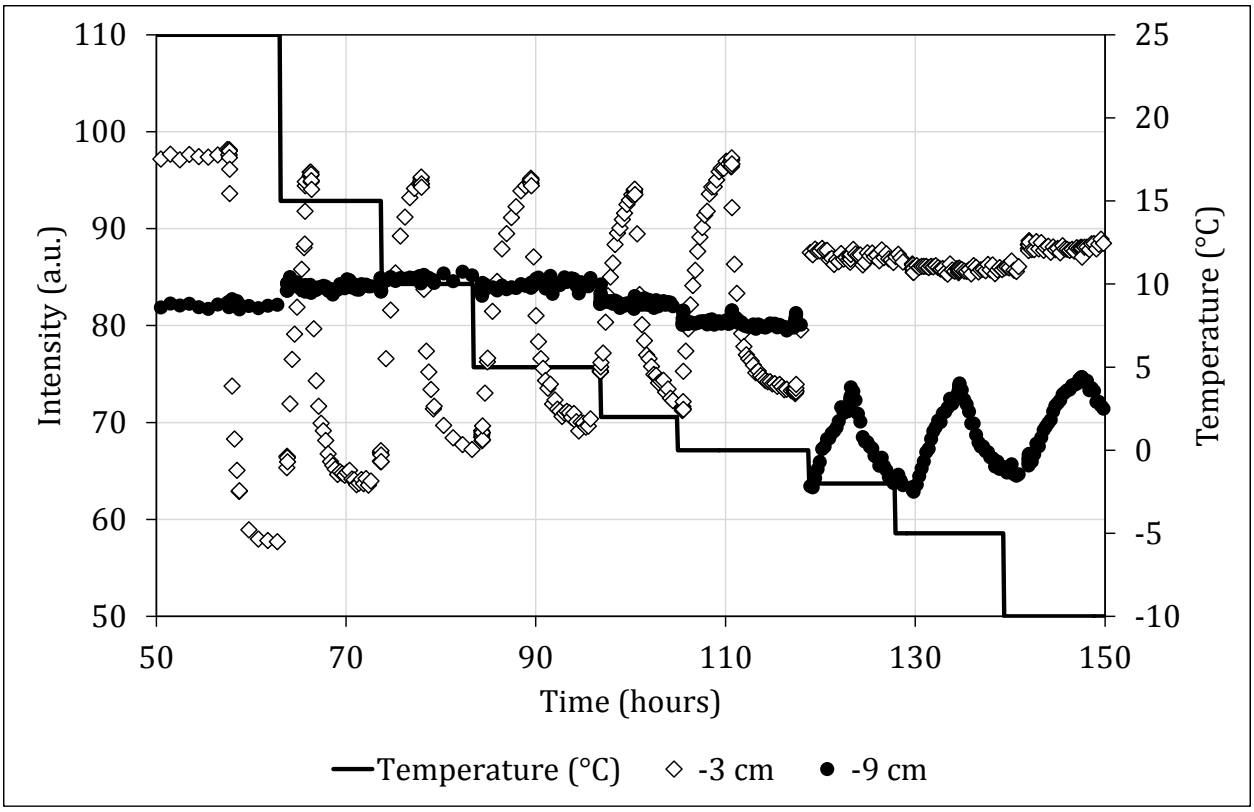

Figure A2: Calibration results from MuFO sensors located within the soil column at depths of -3 cm and -9 cm relative to the soil surface. The water table level was at -9 cm relative to the soil surface. The figure shows that, at temperatures greater than or equal to 0°C, the MuFO sensor at -3 cm responds as expected (high intensity at low oxygen level, lower intensity with increasing oxygen) to variations in oxygen concentrations imposed via alternate sparging of N_2 and air, while the sensor at -9 cm was unresponsive. At sub-zero temperatures, the sensor at -3 cm becomes unresponsive to the oxygen fluctuations, while the sensor at -9 cm showed the expected response, indicating a change in gas migration pathways was physically controlled by the freezing process. Neither of these data sets were used in the final calibration due to the inconsistent response with temperature variation.

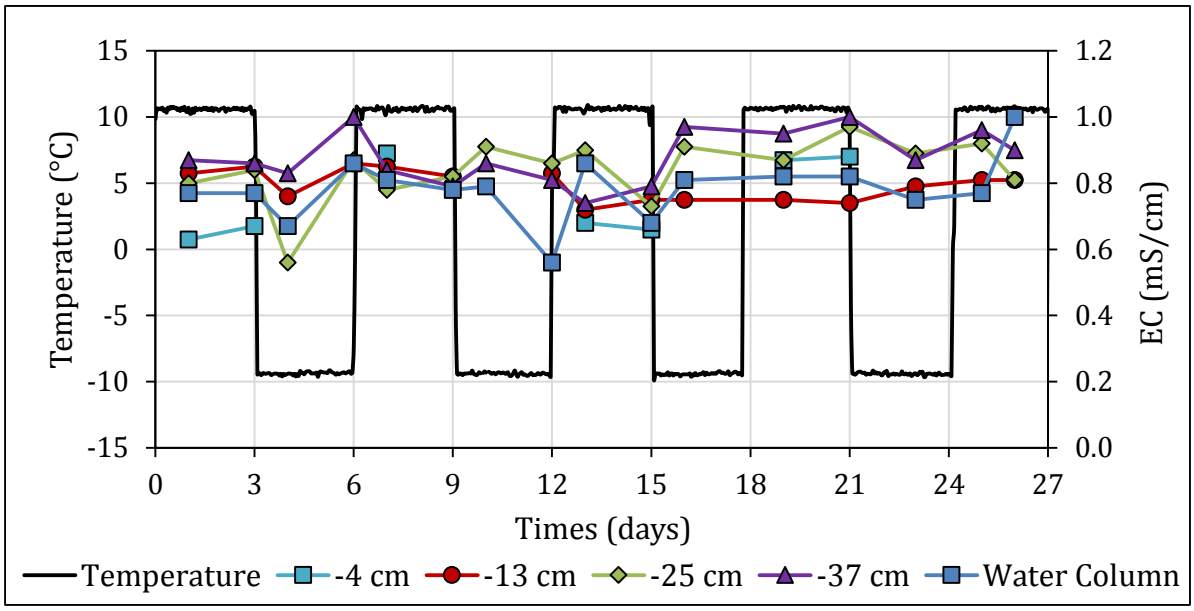

Figure A3: Electrical conductivity (EC) in freeze-thaw column over time, as determined from water samples collected at various depths.

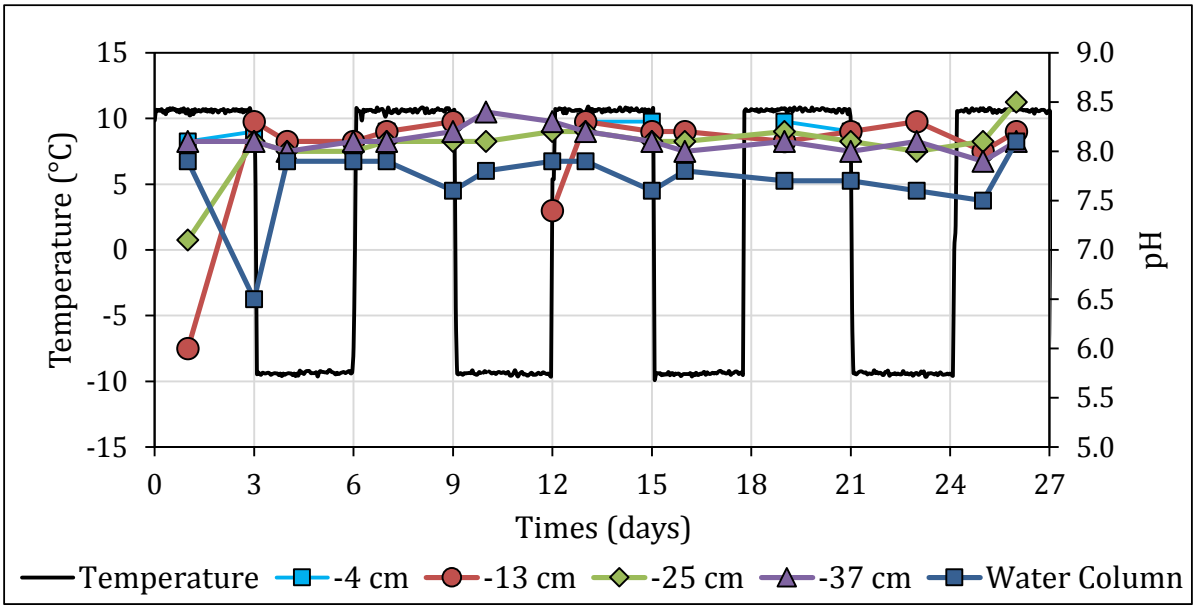

Figure A4: pH values in freeze-thaw column over time, as determined from water samples collected at various depths.

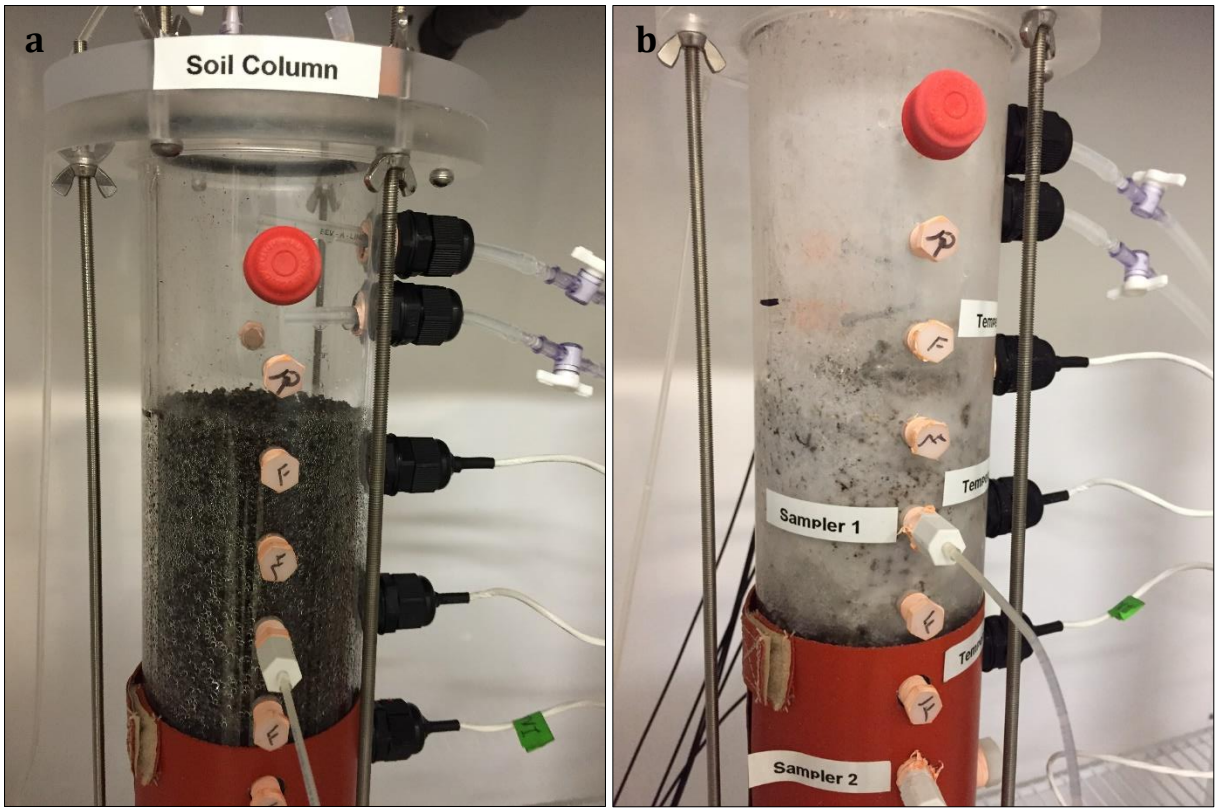

Figure A5: Photograph of soil column from freeze-thaw experiment at the initial thaw (a) and during one of the subsequent frozen periods (b), showing soil freezing in unsaturated area.

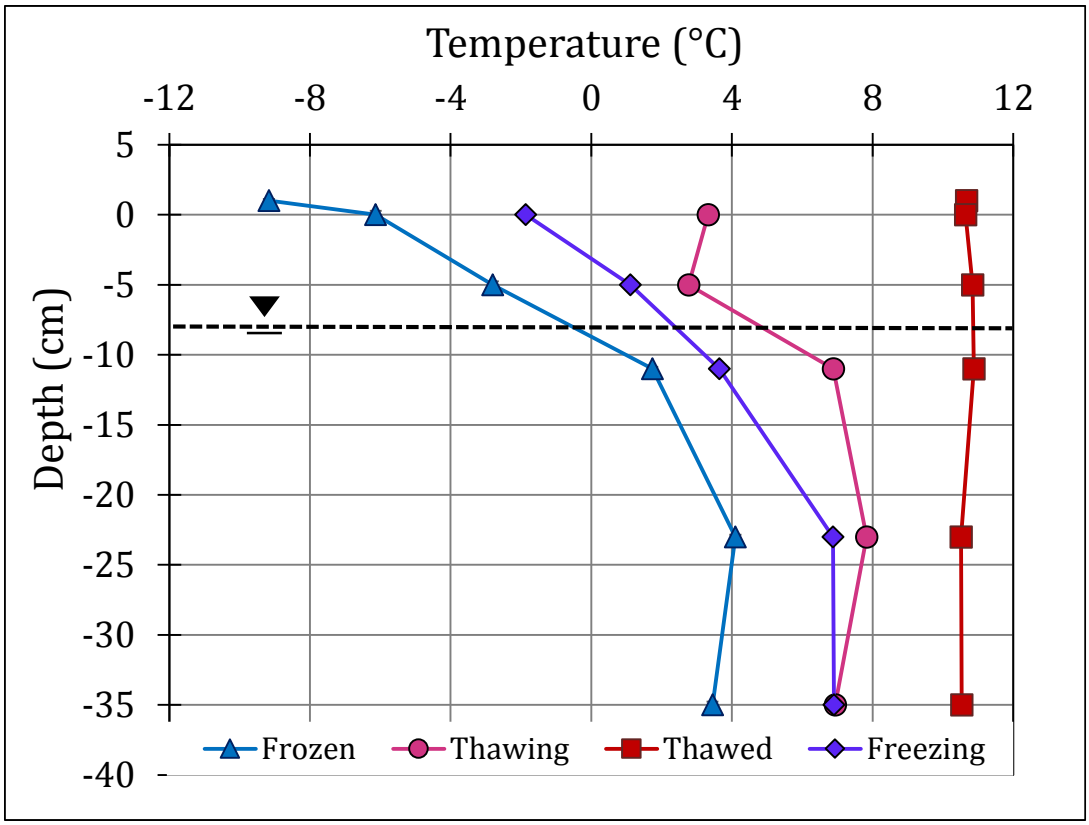

Figure A6: Averaged temperatures recorded during freeze and thaw periods at various soil depths over time. Data point at +1 cm corresponds to the temperature in the environmental chamber.